Earth Planets Space, **57**, 571–590, 2005

Rupture process by waveform inversion using simulated annealing and simulation of broadband ground motions

Yoshiaki Shiba[1] and Kojiro Irikura[2]

[1]*Central Research Institute of Electric Power Industry, 1646 Abiko, Abiko-shi, Chiba 270-1194, Japan*
[2]*Kyoto University, Yoshida, Sakyo-ku, Kyoto 606-8501, Japan*

(Received January 7, 2004; Revised May 17, 2005; Accepted May 18, 2005)

A source inversion method using very fast simulated annealing is proposed to estimate the earthquake rupture process, and associated radiation of broadband strong ground motions. We invert the displacement and velocity motions separately to estimate the spatio-temporal distributions of effective stress and moment. The developed method is applied to the near-source strong motions in the frequency range up to 5 Hz from the 1997 Izu-Hanto Toho-Oki earthquake (MJMA 5.9). Results of the displacement inversion indicate that for this earthquake the seismic moment is mainly released from the shallower region and the northern area from the hypocenter. Similar results are obtained from the velocity inversion, and the variation of the effective stress also exhibits a similar behavior to the moment distribution. Based on the inversion results, we propose a characterized source model that consists of the finite number of asperities and a background area with uniform effective stresses. The broadband ground motion simulation demonstrates that the characterized source model successfully reproduces the observed ground motions in spite of the simplification of actual (inverted) source process. This suggests our proposed inversion method and source characterization process are suitable for the strong-motion prediction that reflects the high-frequency radiation from an actual earthquake.

Key words: Waveform inversion, simulated annealing, empirical Green's function, effective stress, characterized source model.

1. Introduction

When studying earthquake source physics it is important to reveal the rupture process that radiates seismic waves in the broadband frequency range from 0.1 to 10 Hz. Such broadband frequency motions are also of engineering interest for estimating input ground motions used in the seismic design. Since the 1970's a number of researchers have constructed seismic source inversion schemes to obtain kinematic source models from strong-motion data observed near the source region (e.g. Trifunac, 1974; Olson and Aspel, 1982; Hartzell and Heaton, 1983), revealing the complex source rupture process such as the heterogeneous slip distribution. Using inversion results from many past earthquakes, recent studies statistically examine the scaling relation of the "inner" fault parameters that specify the fault heterogeneity, such as the area, moment and effective stress of the asperity as well as that of the "outer" fault parameters that describe the overall faulting such as total rupture area and average stress drop. In these studies the asperity and non-asperity (background) area are categorized systematically based on the objective criterion (Somerville *et al.*, 1999; Mai and Beroza, 2000; Miyakoshi *et al.*, 2000). These studies are often used when source models of the scenario earthquakes are required for the prediction of strong ground motions.

However, in most cases the seismic source inversions have been performed in the frequency range up to 0.5 or 1 Hz. This limitation does not reach the frequency range in which the maximum velocities and accelerations of the strong-motions are implied. This is mainly because the conventional inversion methods employ the theoretical Green's function assuming a laterally homogeneous layered medium, which is inappropriate for evaluating ground motions in the high frequency range. Furthermore, the assumption of a simple shape for slip velocity function and the introduction of smoothing constraints for the stability of the solution (e.g. Hartzell and Heaton, 1983) also underestimate the generation of high-frequency waves. Since the source models inferred from the conventional inversion methods do not include information concerning the high-frequency ground motions, it is necessary for the evaluation of broadband strong motions to find the relationship between the asperity where the slip value is relatively large and mainly low-frequency waves are radiated and the area where mostly high-frequency motions are generated.

One way to examine these issues is to perform the inversion using the envelope shape of high-frequency motions instead of a waveform (e.g. Zeng *et al.*, 1993; Kakehi and Irikura, 1996). The envelope inversion eliminates the phase information of waveforms for the sake of stability of the solutions, and makes it possible to obtain information of the high-frequency radiation. Kakehi and Irikura (1996) applied the inversion procedure to envelopes of acceleration seismograms from the 1993 Kushiro-Oki, Japan, earth-

quake (Mw 7.6) and suggested that high-frequency waves are radiated from regions that are complementary to the area of asperities that emit low frequency waves. In their formulation the inversion result exhibits the distribution of high-frequency radiation intensity. Nakahara *et al*. (2002) conducted the inversion analysis using the envelopes of observed *S*-waves that propagate through a scattering medium to estimate the high-frequency energy radiation from the moderate earthquake (MJMA 6.1; MJMA means the magnitude determined by Japan Meteorological Agency) in Iwate, Japan, based on the radiative transfer theory. They found that the high-frequency energy was strongly radiated from the deepest periphery of the large moment released area, estimated using the low-frequency waveform inversion. In both cases the frequency range in which the envelope inversions are performed is higher than 2 Hz.

On the other hand some other researchers have reported that the observed strong ground motions in the broadband frequency range from about 0.1 Hz to 10 or 20 Hz can be simulated assuming they are radiated from a large slip area. Kamae and Irikura (1998) successfully synthesized near-field strong ground motions of the 1995 Hyogo-ken Nanbu earthquake by forward modeling using the empirical Green's function (EGF) method (Irikura, 1983, 1986). They reconstructed the source model suitable for broadband-frequency ground motions based on the model estimated from low-frequency data (Sekiguchi *et al*., 1996). The new model they constructed for the strong-motion simulation is composed of three independent patches with high stress drop located close to large moment released regions. Miyake *et al*. (1999) also estimated the strong-motion generation areas of two moderate earthquakes occurring in Kagoshima, Japan, on March and May 1997 by forward modeling. For the March event the strong-motion generation areas they estimated agree well with the area of large dislocation deduced using the low-frequency waveform inversion by Horikawa (2001).

Apparently, the high-frequency wave radiation area deduced from the broadband simulation does not always correspond to the area obtained from the envelope inversion, though the frequency ranges to which both methods are sensitive do not completely overlap. It should be noticed that the broadband simulation requires an average source model that can explain not only high-frequency motions such as accelerations and velocities, but also low-frequency displacements. By applying the inversion to the high-frequency waveforms including the phase information, it becomes possible to directly estimate the distribution of source parameters that control the high-frequency radiation, such as effective stress.

In this study we adopt very fast simulated annealing (VFSA) as an inversion algorithm to statistically find the best global solution of a nonlinear nonconvex (multimodal) problem (Ingber, 1989). VFSA is a modified algorithm on simulated annealing (SA, Kirkpatrick *et al*., 1983). The EGF method is used for a forward process of inversion scheme. We apply the developed method to the near-source displacement and velocity waveform data separately in the frequency range up to 5 Hz, including the frequency band in which source processes are inferred by neither the conventional waveform inversion nor the envelope inversion. The spatial distributions of effective stress, seismic moment, rise time and rupture starting time are estimated in the inversion procedures. The target event we choose is the Izu-Hanto Toho-Oki earthquake of March 4, 1997 (MJMA 5.9) and the observed records from its aftershock are used as the empirical Green's functions. Finally we construct the characterized source model that consists of several rectangular asperities and background area for the target event based on the results from the velocity and displacement inversions. Characterized source models are very useful to discuss the statistical feature of earthquake source, which is easily applied to the strong motion prediction. The synthetic ground motions in the frequency range up to 10 Hz are calculated from the characterized source model and the model from the velocity inversion respectively and are compared with the observed motions. We further discuss the scaling relations of the asperity area and the effective stress obtained here with respect to the total seismic moment.

2. Method

2.1 Simulated annealing

Simulated annealing (SA) is a heuristic technique to search a global minimum for the combinatorial optimization problems (Reeves, 1993). SA is based on the algorithm that simulates a physical process of heating and then slowly cooling a substance to obtain a strong crystalline structure (Metropolis *et al*., 1953). Atoms in a substance at high temperatures are able to move freely and keep high-energy states and when the substance is cooled slowly, the atoms line up and form a crystal that is the minimum energy for this system. By connecting these energy states with the objective functions, Kirkpatrick *et al*. (1983) proposed that the SA forms the basis of an optimization technique for combinatorial problems. Recently SA has been introduced to the source inversion by several researchers (e.g. Ihmlé, 1996; Delous *et al*., 2000, 2002; Ji *et al*., 2002a, 2002b).

The inversion procedure based on the SA is performed as follows. First, we represent the objective function (or the misfit) to be minimized for the problem. It is usually defined as the L1 or the L2 norm of the residuals between calculated values and observed data. The model parameters are initialized randomly within the prescribed search area and the current misfit is calculated. Then, a random change from the neighborhood of the current state-space is imposed on one parameter and the corresponding change in the misfit is also evaluated. The algorithm of SA accepts not only changes that decrease misfit but also some changes that increase it. The latter are accepted with a probability based on the Boltzmann distribution.

$$P(T, \Delta E) = \exp(-\Delta E/T) \tag{1}$$

where the "temperature" T is a control parameter and ΔE is a change in the misfit. This formulation is known as the Metropolis algorithm. This procedure allows the system to jump out of the local minima and find the global one according to the probability controlled by the temperature T as shown above. The iteration starts from a sufficiently high temperature at which both positive and negative values of

ΔE are accepted, and then T is lowered through the iteration to the value where the movement to the high-energy state is unlikely to occur. Geman and Geman (1984) proved SA guarantees an optimal solution (a global minimum) if the temperature T is decreased slower than a logarithmic manner such as,

$$T(k) \geq \frac{N\Delta}{\log(1+k)} \tag{2}$$

where k is cooling time and N is the number of model parameters. Δ is the difference between the maximum energy produced by any possible configuration and the energy at the deepest local minimum. Δ represents the height of the energy which is necessary to escape from one local minima to another one.

In this study we employ the very fast simulated annealing (VFSA) proposed by Ingber (1989). VFSA permits the temperature T decreasing exponentially in k,

$$T(k) = T_0 \exp\left(-qk^p\right) \tag{3}$$

where T_0 is an initial temperature, p and q are appropriate constants. The cooling schedule of VFSA (Eq. (3)) is faster than the conventional one cited above, and it statistically finds a global minimum. The i-th model parameter m_k^i at cooling time k is calculated with a variable y^i and the previous parameter m_{k-1}^i,

$$\begin{aligned} &m_k^i = m_{k-1}^i + y^i\,(B_i - A_i) \\ &m_k^i \in [A_i, B_i]\,,\ y^i \in [-1, 1] \end{aligned} \tag{4}$$

where A_i and B_i respectively are the lower and upper limits of search area for the i-th parameter. In VFSA the generation of variable y^i that obey the Cauchy distribution is dependent on the temperature T at that time as follows,

$$\begin{aligned} &y^i = sgn\left(u^i - 1/2\right) T(k) \left[(1 + 1/T(k))^{|2u^i - 1|} - 1\right] \\ &u^i \in U[0, 1] \end{aligned} \tag{5}$$

where u^i is a random variable that is generated from the uniform distribution, and the sgn function is 1 when the argument is positive and is -1 when the argument is negative.

The structure of the SA algorithm is relatively simple, and there are few restrictions for the choice of the objective functions because the SA does not require differential coefficients. In order to derive the high-frequency radiation based on the waveform fittings it is important to identify the amplitude and correct timing of the distinct phase implied in the observed high-frequency motions with the effective stress and rupture starting time on the fault plane. Since the rupture time has a nonlinear dependence on the waveforms, we need to use a nonlinear inversion technique. SA or VFSA is available for such problems including strong nonlinearity, because SA has high ability to avoid the local minima and find the global minimum in the nonlinear search space.

As an alternative search algorithm based on the heuristic technique, a genetic algorithm (GA; Holland, 1975) is often applied for the inversion method in the field of geophysics. Yamanaka (2001) applied VFSA to the inversion of surface wave phase velocity, and compared its performance with that of GA. They showed VFSA finds models that are much closer to the global minimum solution than GA within acceptable computational costs. In this paper we also compare the performance of VFSA with other heuristic methods in the numerical tests.

2.2 Formulation of forward process

The application of the EGF method as a forward process of inversion is based on a review of previous studies. The idea of using observed records of a small event occurring near the source region of a large earthquake as an EGF was originally introduced by Hartzell (1978). Irikura (1983, 1986) combined this approach with the scaling relationship of source parameters (Kanamori and Anderson, 1975) and the similarity law of source spectra (Aki, 1967) to obtain physically reliable results when simulating strong motions. Several researchers have proposed inversion procedures using an EGF. Fukuyama and Irikura (1989) and Fukuyama (1991) estimated the rupture starting time, moment release, and rise time of the target event using an EGF and a nonlinear inversion technique, and discussed the relationship between the heterogeneous rupture process of a large earthquake and the aftershock distribution or the geological structures in the source region. Hellweg and Boatwright (1999) determined the stress drop and the rupture time of moderate earthquakes based on the filtering technique developed by Boatwright (1988). Mori and Hartzell (1990) used the deconvolution technique with an EGF to deduce the relative source time function to the EGF for a moderate earthquake, and estimated the slip distribution by using the least squares inversion. Okada *et al.* (2001) and Ide (1999, 2001) investigated the rupture process of the moderate earthquake using the multiple time-window technique (Hartzell and Heaton, 1983; Ide and Takeo, 1997) and empirical Green's functions instead of theoretical ones in order to analyze high-frequency waveforms.

In this study we adopt the formulation of the EGF method developed by Irikura (1983, 1986). In the EGF method the fault plane of the target event is divided into sub-faults having same area. The scaling parameter N, which is a square root of the number of sub-faults, is related to the seismic moment and the effective stress as follows,

$$CN^3 = \frac{M_o}{m_o} \tag{6}$$

where M_o and m_o respectively are the seismic moment of the target event and the small event used as the empirical Green's function (hereafter referred to as the element event). C denotes the ratio of effective stress between them. The ground motions from the element event are superposed assuming that they are radiated from each sub-fault with a time delay according to the rupture propagation and the geometrical relation between the fault plane and the observation station. The ground motion from the element event is convolved with the appropriate filter function to correct the difference of the slip velocity time function between the target and element event. Here we adopt two types of filter functions for inverting displacement and velocity motions respectively, as shown in Fig. 1. Following Fukuyama and

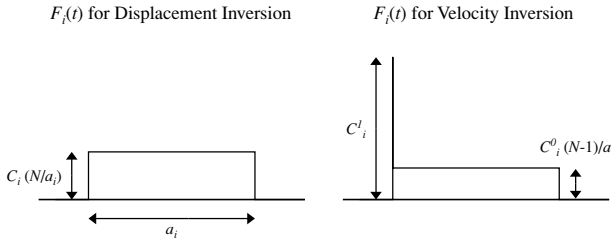

Fig. 1. A schematic illustration of the filter function $F(t)$ used in the empirical Green's function method. In the displacement inversion $F(t)$ is a boxcar function (left). The height of $F(t)$ is proportional to the moment density ratio $C_i N$ between the target event and the small event, and its duration corresponds to the rise time of the target event a_i. We estimate the parameters C_i, a_i and rupture-time perturbation s_i. In the velocity inversion the filter function is composed of a delta function and a boxcar function (right). The height of a delta function C_i^1 is equal to the effective stress ratio.

Irikura (1989), the filter function for the displacement inversion is expressed by a boxcar function,

$$\begin{aligned} F_i(t) &= C_i\,(N/a_i)\,H\,(t-t_i)\,[1-H\,(t-t_i-a_i)] \\ t_i &= (r_i-r_0)\,/\beta+\xi_i/v_0+s_i \end{aligned} \tag{7}$$

where C_i is the weighting factor and characterizes the average effective stress ratio of the i-th sub-fault of the target event to the element event. Then $C_i N$ represents the ratio of the released moment from the i-th sub-fault to that of the element event. a_i is the rise time. r_0 and r_i respectively are the distance from the hypocenter and i-th sub-fault to the observation station. ξ_i is the distance from the hypocenter to i-th sub-fault and v_0 is the assumed constant rupture velocity. s_i is perturbation from the rupture time ξ_i/v_0. β is the S-wave velocity. $H(t)$ represents the Heaviside step function, which is 1 for $t \geq 0$, and is 0 for $t < 0$. Since the integration of $F_i(t)$ with respect to t is equal to $C_i N$, the convolution with the filter function $F_i(t)$ gives $C_i N$ times larger spectral amplitude in the lower limit of frequency, assuring the suitable moment ratio between each sub-fault of the target event and the element event. In the displacement inversion we estimate three model parameters C_i, a_i and s_i. The total moment of the target event M_o is estimated by

$$M_o = m_o N \sum_{i=1}^{M} C_i, \tag{8}$$

where M represents the number of sub-faults and is usually equal to N^2, though in case of source inversion M is often set to be larger than N to retain the appropriate search space for the inversion procedure.

For the representation of high-frequency radiation, the use of $F_i(t)$ defined in Eq. (7) is inappropriate, because the Fourier spectrum of a boxcar function decays in proportion to ω^{-1}, where ω denotes the angular frequency. The ω^{-2} model providing the shape of source spectrum based on the scaling law (Aki, 1967) requires that the high-frequency asymptote of $F_i(\omega)$ goes to C_i (Irikura, 1986). To satisfy this condition Irikura (1986) proposed a new type of the filter function to which the Dirac delta function $\delta(t)$ is added as follows,

$$\begin{aligned} F_i(t) = C_i\{&\delta(t-t_i) \\ &+[(N-1)/a_i]H(t-t_i) \\ &\cdot[1-H(t-t_i-a_i)]\}. \end{aligned} \tag{9}$$

A time integral of $F_i(t)$ agrees with the released moment ratio $C_i N$ in Eq. (9) as well as in Eq. (7). Furthermore the amplitude of the Fourier spectrum $F_i(\omega)$ becomes C_i in the high-frequency asymptote due to the contribution of the delta function. Therefore the filter function (9) ensures the scaling relation between the target and the element event in both the high frequency and low frequency range. It also should be noticed that the synthesized slip velocity time function of the target event using Eq. (9) roughly resembles the slip velocity derived from the dynamic source rupture modeling (e.g. Day, 1982), so that the calculated ground motions are expected to preserve physically acceptable characteristics in the broadband frequency range. In this study we modify Eq. (9) for the velocity inversion to estimate the amplitude of the delta function and that of the following boxcar function individually,

$$\begin{aligned} F_i(t) = C_i^1\delta\,(t-t_i) &\\ +C_i^0\,[(N-1)\,/a_i] &\\ \cdot H\,(t-t_i)\,[1-H\,(t-t_i-a_i)]\,. & \end{aligned} \tag{10}$$

In the velocity inversion we estimate C_i^0, C_i^1 and the rupture-time perturbation s_i (see Eq. (7)) of i-th sub-fault. The model parameter C_i^1 is interpreted to stand for the intensity of high-frequency radiation and C_i^0 represents the amplitude of intermediate and low frequency motions. The rise time a_i is specified by using the results from the displacement inversion. Note that the effective stress ratio of the i-th sub-fault of the target event to the element event is equivalent to C_i^1, which is the coefficient of the delta function, and the moment ratio between them is derived from the time integral of Eq. (10), i.e. $C_i^1 + C_i^0(N-1)$

In both the displacement and velocity inversion, we impose a constraint on the rupture-time perturbation s_i to suppress the instability of solutions. Following Yoshida and Koketsu (1990) and Horikawa (2001), the constraint for the rupture propagation is expressed as

$$\nabla^2 s_i = 0, \tag{11}$$

where ∇^2 is a discrete Laplacian operator. The VFSA inversion is performed by minimizing the misfit to data and the constraint shown in Eq. (11). A relative weighting factor W is introduced into the minimization process to obtain the best-balanced solution that satisfies both realistic rupture propagation and small misfit to waveforms. The resultant inversion criteria can be represented as

$$E + W \cdot \sum_i \nabla^2 s_i = \text{minimum}, \tag{12}$$

where E denotes the misfit, which is given by the L1 or L2 norm of the residuals between the synthetic and observed ground motions. For one waveform the misfits using the L1 norm E_{L1} and the L2 norm E_{L2} are described as

$$\begin{aligned} E_{L1} &= \sum_{i=1}^{ntm} |u_s\,(t_i) - u_o\,(t_i)| \Big/ \left\{\sum_{i=1}^{ntm} (u_o\,(t_i))^2\right\}^{1/2} \\ E_{L2} &= \sum_{i=1}^{ntm} (u_s\,(t_i) - u_o\,(t_i))^2 \Big/ \sum_{i=1}^{ntm} (u_o\,(t_i))^2\,, \end{aligned} \tag{13}$$

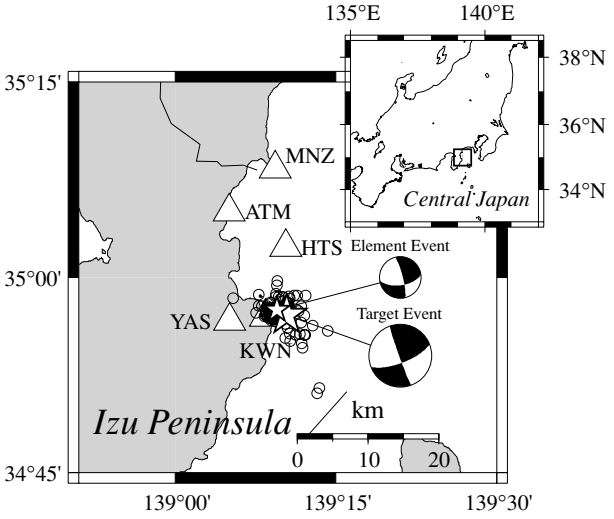

Fig. 2. Map showing the epicenter of the target event (large open star), element event (small open star) and other aftershocks (open circles). The focal mechanisms of the target and element events are also shown. The open triangles indicate the strong motion stations on the rock outcrops used in this study.

Table 1. The initial source parameters of the target and element events used for the inversion.

Target event	
Origin time (JST)	1997/3/4 12:51:27
Latitude (deg. N)	34.952
Longitude (deg. E)	139.173
Depth (km)	2.64
MJMA	5.9
Strike (dig.)	160
Dip (dig.)	87
Sub-fault size (km)	1.9
Rise time ratio N	3
Number of sub-faults M	5×5

Element event	
Origin time (JST)	1997/3/5 22:43:29
Latitude (deg. N)	34.959
Longitude (deg. E)	139.158
Depth (km)	3.3
MJMA	4.9
Seismic moment ($\times 10^{15}$ Nm)	8.35
Stress Drop (MPa)	3.11

where u_s and u_o are the synthetic and observed ground motions respectively. ntm is the number of data points. In later section we will compare the ability of finding true parameters for E_{L1} and E_{L2} in the numerical tests.

Though many researchers have adopted a spatial smoothing constraint for slips or slip velocities together with that for time variables, we do not employ additional constraints to ensure free spatial distribution of other model parameters. Only the nonnegative constraints for the moment and the effective stress are included in the choice of lower limit of search area, A_i in Eq. (4).

3. Data

We applied the developed VFSA inversion to strong-motion data recorded at bedrock stations during the 1997 Izu-Hanto Toho-Oki earthquake (MJMA 5.9). The target event was the largest within the moderate earthquake swarm occurring over a several-day period in March, 1997 (JMA, 1997). We used the records from the following small event (MJMA 4.9) for the empirical Green's function (the element event). In general high-frequency radiation from the seismic source can be investigated more minutely by choosing a smaller EGF, because the size of sub-fault becomes smaller. However, the number of observed records from such a small event is not often enough for the inversion analysis. Furthermore, the lower limit of the frequency band available for the inversion analysis is restricted by the signal-to-noise ratio of the observed EGF. In the EGF method the high-frequency radiation whose wavelength is shorter than the grid-size for the inversion is contained in the element event itself, hence it is represented statistically by superposing the employed EGF. In Fig. 2 the epicenters of the target event, element event and other aftershocks occurring within one day are shown with the distribution of observation stations we analyzed. Their hypocentral locations were determined by JMA and the focal mechanisms were published by F-net (Fukuyama *et al.*, 1998). All of the stations are on rock outcrops with three-component force-balanced accelerometers operated by the Central Research Institute of Electric Power Industry (CRIEPI). The observed acceleration records were band-pass-filtered from 0.4 to 5 Hz, and then numerically integrated to obtain data for the velocity and displacement inversions. We prepared two initial fault models as shown in Fig. 3 based on the aftershock distribution. The source parameters for the inversion are shown in Table 1. The S wave velocity of 3.2 km/s in the source region was estimated by taking an average of the S wave velocity structures proposed by Takeo (1988). From the aftershock distribution in depth we determined the upper limit of the seismogenic zone to be the depth of 0.5 km. In model (a) we located the hypocenter in the middle of the strike direction and in the shallowest part along the dip direction as seen in Fig. 3. In model (b) the hypocenter is located on the deep adjacent mesh. In this model the edge of the fault reaches the upper border of the seismogenic zone. Then the focal depth, which is assumed to be located on the center of the mesh, is set on the slightly deeper position due to the fixed size of the sub-fault that is equivalent to the fault dimensions of the element event. We performed the VFSA inversion using these two initial models and adopted the better model by comparing the fit between the synthetic ground motions and the observed ones.

To estimate the fault dimension of the target and element events we here applied the spectral inversion technique proposed by Iwata and Irikura (1988) and derived the source spectra of these events. Then by fitting the theoretical spectrum of the ω^{-2} model (Aki, 1967; Brune, 1970, 1971),

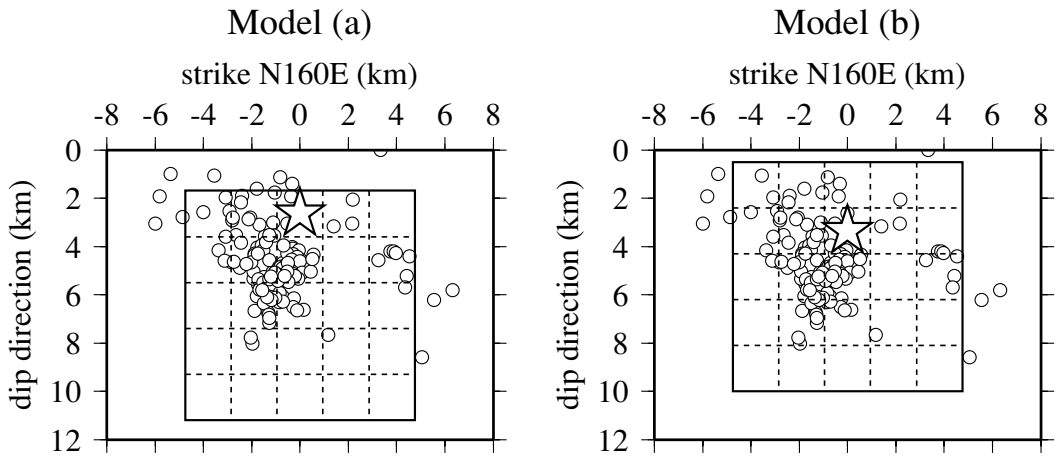

Fig. 3. Assumed fault models for the inversion analysis. Star indicates the hypocenter. Open circles show the hypocenters of aftershocks determined by JMA.

we obtained the rough estimates of the fault radii of these events. The rise time ratio N, which is equal to the scale parameter shown in Eq. (6), is directly determined from the ratio of fault size between the target and element events. The number of sub-faults M was set to be $(N+2)^2$ by adding columns and rows around the N^2 fault area.

The radiation patterns were not corrected in this analysis because the fault orientation of the element event was similar to that of the target event. However for the stations located close to the extension of nodal planes of the fault, the radiation patterns of two horizontal components are calculated for the target and element event respectively. The effect of the radiation pattern on the inversion result is discussed in later sections. The frequency dependence of the attenuation factor for the S-waves, $Q_S(f)$, is assumed as $Q_S(f) = 130 f^{0.7}$ for $f \geq 1$ Hz, which is obtained by Kinoshita (1994) in the crust of the Southern Kanto area including the source region in this study.

Since all model parameters except for the rise time are the ratios to those of the element event in our inversion scheme, it is necessary to accurately determine the values of these parameters for the element event in advance in order to discuss the physical faulting process of the target event. The seismic moment of the element event m_o is estimated from the low-frequency asymptote of the displacement source spectrum obtained from the spectral inversion analysis. The total seismic moment of the target event is also deduced from this analysis, so we can use it for the comparison with results of inversion. The stress drop $\Delta\sigma$ of the element event is estimated assuming a circular fault (Eshelby, 1957) as follows,

$$\Delta\sigma = \frac{7}{16}\frac{m_o}{r^3} \tag{14}$$

where r denotes the source radius deduced from the spectral inversion. We assume that the effective stress σ_e related to high-frequency motions is equal to the stress drop $\Delta\sigma$ (Brune, 1970, 1971).

4. Inversion Results

4.1 Numerical tests

To examine the validity of the developed inversion method, we applied it to the ground motions synthesized from an artificial fault model. Two different fault models were prepared for the displacement inversion and the velocity inversion, respectively as shown in the upper part of Figs. 4 and 5. In the lower part of Figs. 4 and 5 we show the best three solutions out of ten attempts using the appropriate control parameter for inversion procedure discussed later in this section. The model for the displacement inversion includes two distinct asperity areas of the same released moment. The moment release from the background area is set to be zero. The rise time of the shallow asperity is twice as long as that of the deep asperity. It should be noticed that we display the weight C_i as the "normalized" moment ratio instead of $C_i N$ in the left column of Fig. 4. When $C_i = 1$ over the entire fault of the target event, the total released moment corresponds to the value expected from the scaling relation of seismic source (Kanamori and Anderson, 1975) with uniform effective stress (or stress drop), therefore the distribution of C_i indicates the discrepancy in the moment release from a homogeneous source of the same magnitude. For the velocity inversion there are also two distinct asperities on the model fault. As seen in Fig. 5 the shallow asperity shows half the effective stress compared with the deep asperity, but twice as large as the parameter C_i^0 that controls the amplitude of boxcar function. Furthermore the effective stress ratio C_i^1 is doubled at one mesh within each asperity. A constant rupture velocity of 0.8 β is assumed for both models. The station distribution and other initial parameters required for the inversion procedure are equivalent to those in the actual situation introduced above. Note that for the fault geometry and the hypocenter location we adopted the parameters for the assumed fault model (b).

Velocity and displacement ground motions from an element event were simulated stochastically as proposed by Boore (1983), assuming a point source and the ω^{-2} spectral model, and they were superposed using the EGF method. Then, adding random noise with zero mean and standard deviation of 5% relative to the peak amplitudes, the syn-

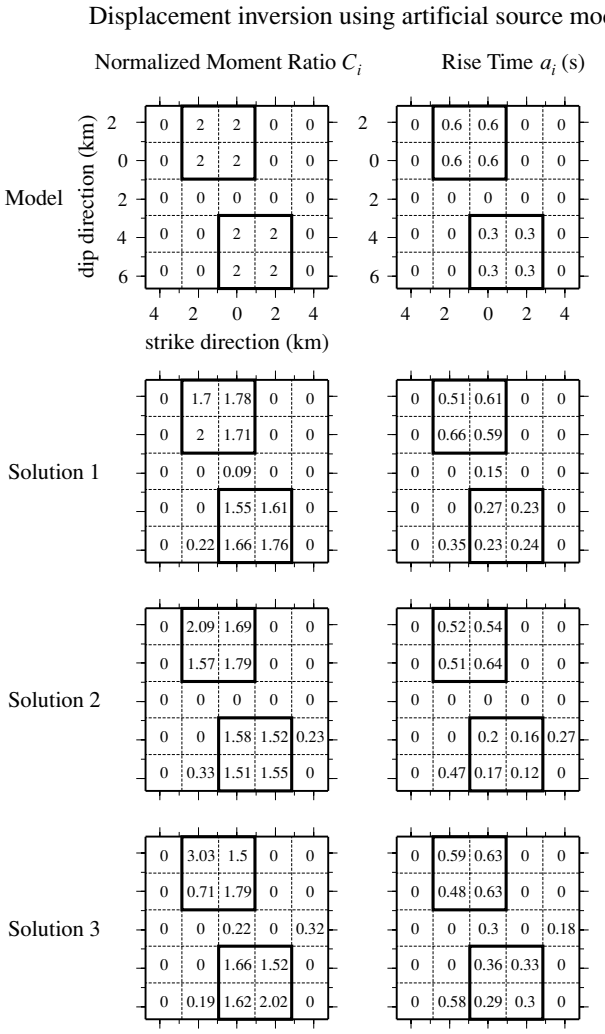

Fig. 4. Spatial distributions of the normalized moment ratio and the rise time of the artificial fault model used in the numerical test for the displacement inversion (upper two figures), and the three best inversion results with smaller L1-norm misfits (lower six figures). Two squared areas enclosed by thick solid lines indicate asperities with different rise times. The moment is released from only the asperity areas in this test model.

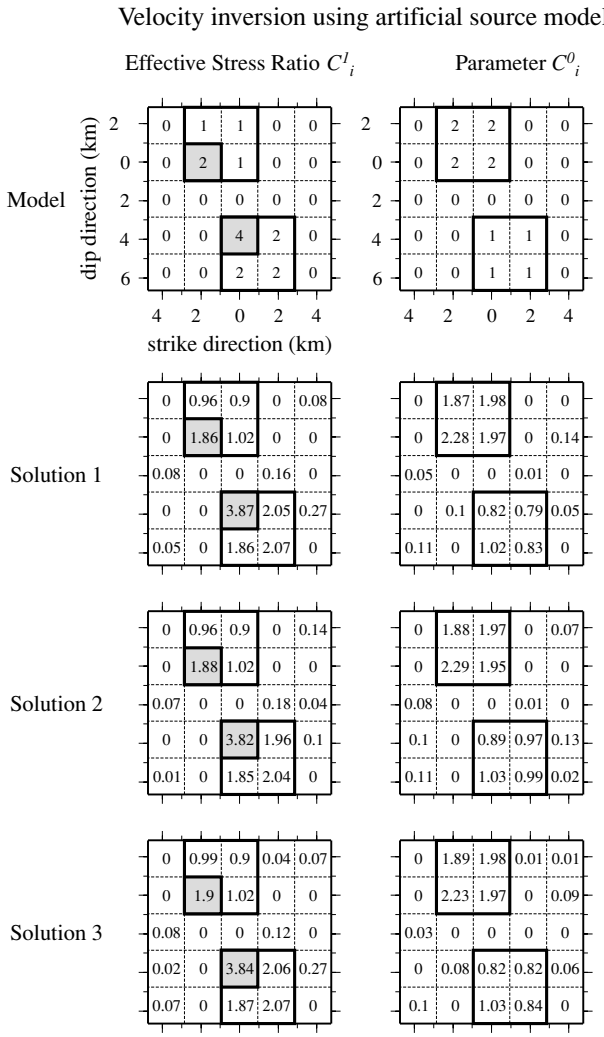

Fig. 5. Spatial distributions of the effective stress ratio C_i^1 and the parameter C_i^0 that is proportional to the amplitude of the boxcar function used for the numerical test in the velocity inversion (upper two figures), and the three best inversion results with smaller L2-norm misfits (lower six figures). The assumed source model consists of two distinct asperity areas (squares enclosed by thick solid lines) and only the peak slip velocity is doubled at one mesh within each asperity displayed as the gray-shaded area.

thetic data set was prepared. Since our concern is S-waves, we used the two horizontal components. Each seismogram was band-pass-filtered from 0.1 to 5 Hz, and the sampling interval was reduced to 0.05 s in order to save computation time. The search areas of model parameters are shown in Table 2. We determined the search area of rupture-time perturbation s_i from the variation in the rupture velocity. When v_1 and v_2 are the lower and upper limits of rupture velocities respectively, the search area of s_i is obtained by

$$\begin{aligned} s_{1i} &\le s_i \le s_{2i} \\ s_{1i} &= \xi_i/v_2 - \xi_i/v_0 \\ s_{2i} &= \xi_i/v_1 - \xi_i/v_0, \end{aligned} \tag{15}$$

where ξ_i is the distance from the hypocenter to the i-th subfault and v_0 is the constant rupture velocity of the assumed model as seen in Eq. (7). Several experimental attempts are performed before the inversion in order to determine the parameters for the cooling schedule. We have to choose the initial temperature T_0, the coefficients p and q that control the cooling speed defined in Eq. (3), and the criterion to terminate the iteration. We specified the initial temperature as the sum of the averaged misfit $\langle E \rangle$ and the standard deviation $sd(E)$ over 100 calculations using random configurations of models, as proposed by Gibert and Virieux (1991)

Table 2. Search areas of model parameters in numerical tests.

Displacement inversion		
C	a (s)	v/β
0.0–5.0	0.0–1.0	0.7–0.9

Velocity inversion		
C^0	C^1	v/β
0.0–4.0	0.0–10.0	0.7–0.9

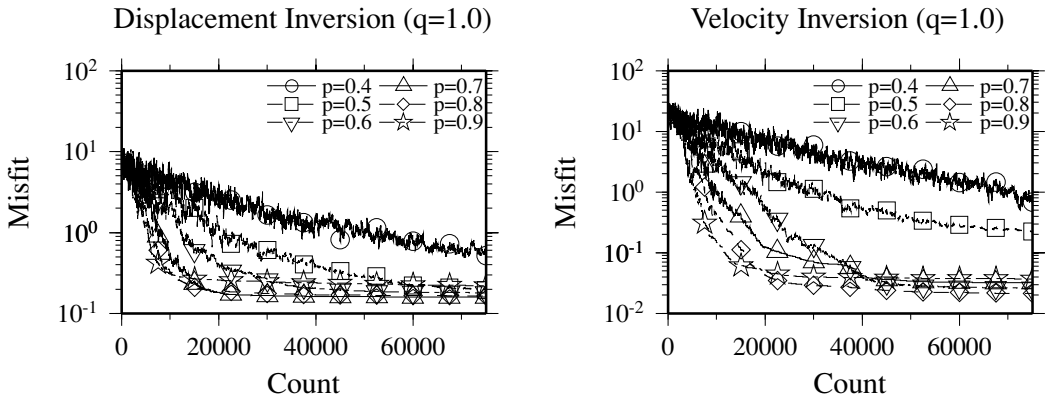

Fig. 6. Variation of misfits with different p values in Eq. (3). Note that the misfits displayed here are the L1 norms for the displacement inversion and the L2 norms for the velocity inversion, respectively. We employed these norms in the following practical analyses.

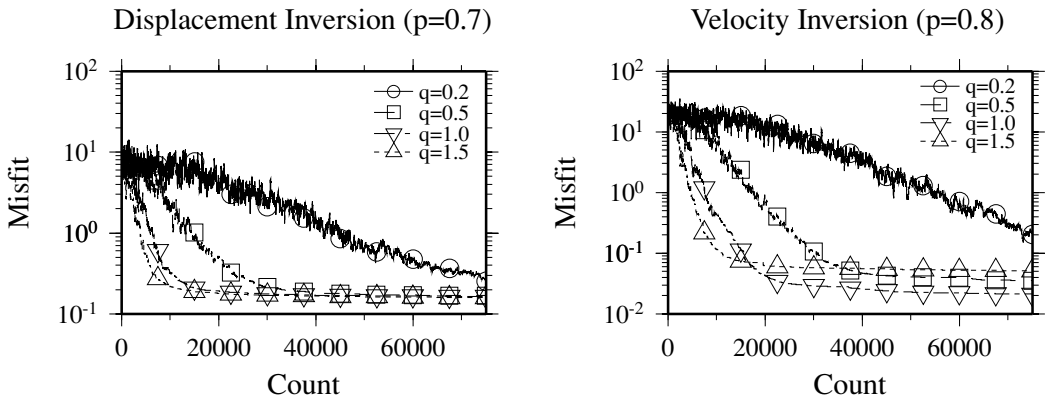

Fig. 7. Variation of misfits with different q values in Eq. (3). The selected norms for the misfits are same as Fig. 6.

such that,

$$T_0 = \langle E \rangle + sd(E). \tag{16}$$

To determine the lowering speed of the temperature, the test runs were made with changing the value of the coefficients p and q in Eq. (3). Figure 6 shows the variations of misfits with lowering the temperature in the displacement and velocity inversions when the coefficient p in the cooling schedule is varied from 0.4 to 0.9 with fixed q of 1.0. We can see the amplitude of the misfit function drops rapidly just after the beginning of iteration as the value of p increases. However as the iteration count progresses the misfit with the cooling schedule using large p of 0.9 does not reduce sufficiently due to few opportunities to accept new parameters that might lead to the global optimal solution. Hereafter we use $p = 0.7$ for the displacement inversion and 0.8 for the velocity inversion. In Fig. 7 we show the case of varying q with fixed p. The cooling schedule using $q = 1.0$ is the most suitable in the velocity inversion for the search of the optimal solution, and that with $q \geq 0.5$ is appropriate in the displacement inversion. Therefore we use $q = 1.0$ hereafter for both inversions. Finally we determined the critical temperature T_c following the suggestion of Ihmlé (1996) and Gibert and Virieux (1991),

$$T_c = K \,\mathrm{var}(noise) = K \,\mathrm{var}(E) \tag{17}$$

where K is an appropriate constant determined through several test runs. Once the temperature reaches T_c, the parameter search is repeated with remaining the temperature at T_c. As pointed out by Mosegaard and Tarantola (1995), when the definition of misfit is the L2 norm and K in Eq. (17) is equal to 1, the iterative search at the critical temperature T_c in the Metropolis algorithm provides the model sampling according to the posterior probability distribution in the Bayesian approach with Gaussian noise. In this study we assume K ranges from 0.1 to 0.5 to ensure reliable convergence. The algorithm terminates when a preset number of iterations have been completed. In this study the number of iterations at the same temperature was set to 10 until the temperature is lowered to T_c. Further the total number of iterations was set to 74,000. Since the number of model parameters is 25 (the number of sub-faults) $\times$ 3 (C_i, a_i and s_i for the displacement inversion, and C_i^0, C_i^1 and s_i for the velocity inversion) $-$ 1 (s_i at the rupture starting mesh) = 74, 1,000 iterations were performed for each parameter. The appropriate weight for the smoothing constraint on the rupture time was examined by performing some preliminary inversions. In practice the solution of the VFSA inversion is not completely independent on the initial values for generation of random numbers due to finite iterations. Therefore we performed 10 inversions with different initial values, and examined the dispersion of solutions and the discrepancy from the true models.

We show the averages and the standard deviations of

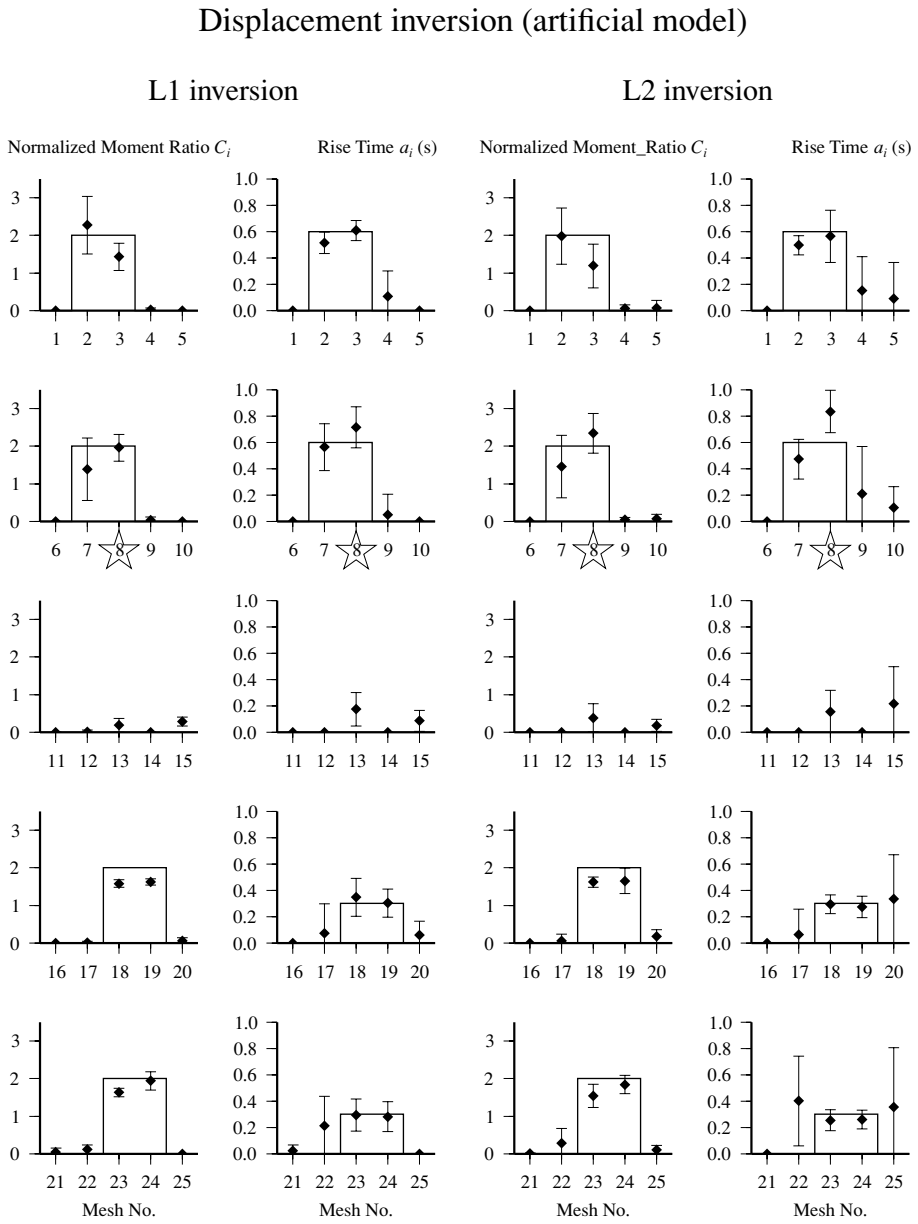

Fig. 8. Averages and the standard deviations of estimated parameters in the displacement inversion, which are obtained from 10 attempts with different initial values in random number generators. Horizontal axis indicates the mesh number of the target fault, measured from the northern shallowest mesh to the strike direction. 8th mesh marked with star indicates the hypocenter. Continuous solid lines show the parameter distribution of the assumed model.

parameters estimated from the displacement inversion in Fig. 8, and those from the velocity inversion in Fig. 9, along with the initially assumed models drawn by solid lines. We found that the source parameters estimated from both inversions agree well with those of the models. In particular the results from the velocity inversion reproduce the model almost precisely and the standard deviations are very small, especially in case using the L2 norm as the misfit function. While the estimated parameters in the displacement inversion show larger fluctuations compared to the case of velocity inversion. The incorrect values of rise times are obtained at surrounding meshes of asperities. This is because the variation of rise time is insensitive to that of the synthetic ground motion when the released moment at the corresponding mesh is small. At the outside of asperity area, the displacement inversion minimizing the L2 norm yields larger estimation error of rise time than that minimizing the L1 norm, as shown in Fig. 8. On the other hand the velocity inversion using the L2 norm minimization provides better solutions than that with the L1 norm in estimation of the effective stress at the deep asperity.

Considering the results from numerical tests, we employ the L1 norm minimization for the displacement inversion owing to good estimation of the rise time distribution especially in the low moment-release area. For the velocity inversion we use the L2 norm minimization showing the good fit to the model. The issue concerning the selection of type of norm is further discussed later. The evolutions of the misfit functions during 10 attempts of the displacement and velocity inversions are shown in Fig. 10. The variance

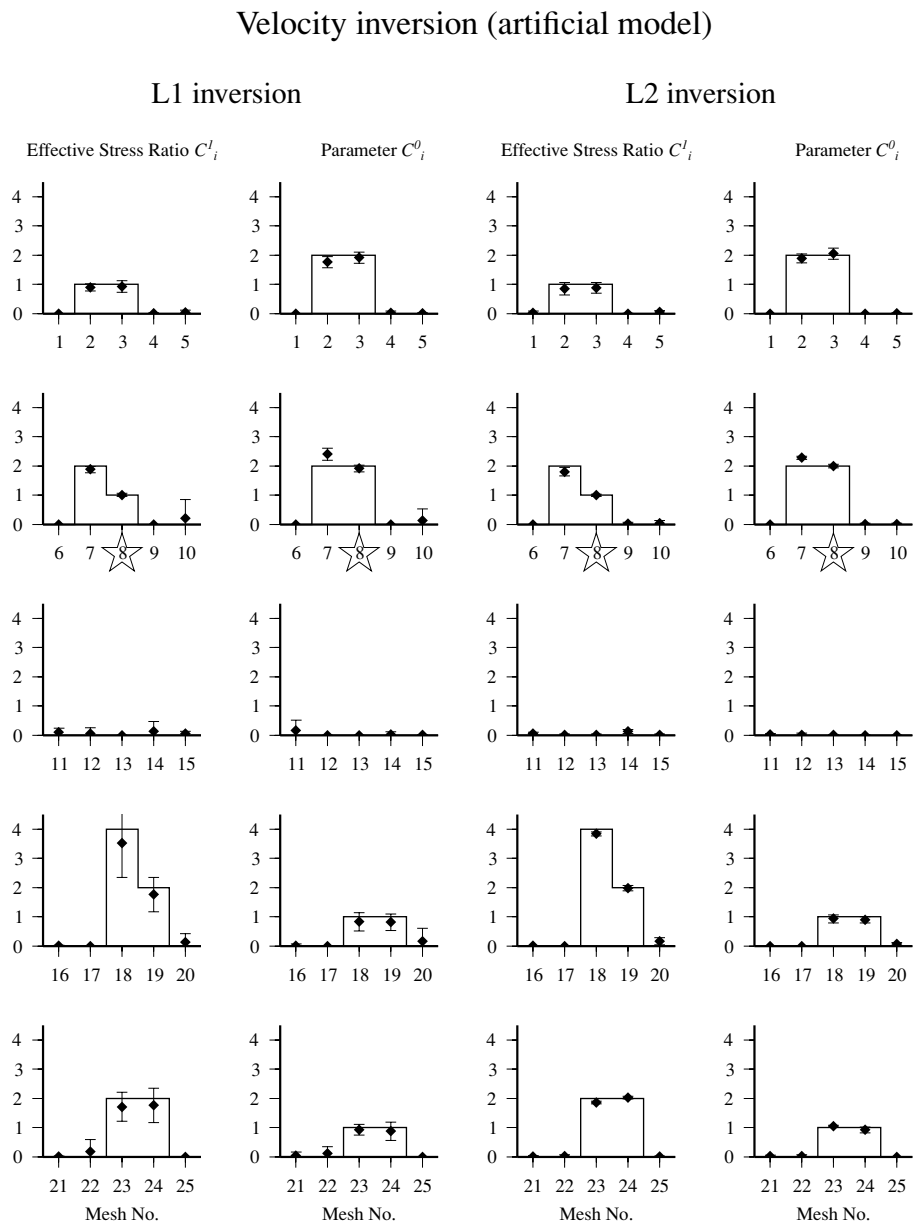

Fig. 9. Averages and the standard deviations of estimated parameters in the velocity inversion. 8th mesh marked with star indicates the hypocenter. Continuous solid lines display the parameter distribution of the assumed model.

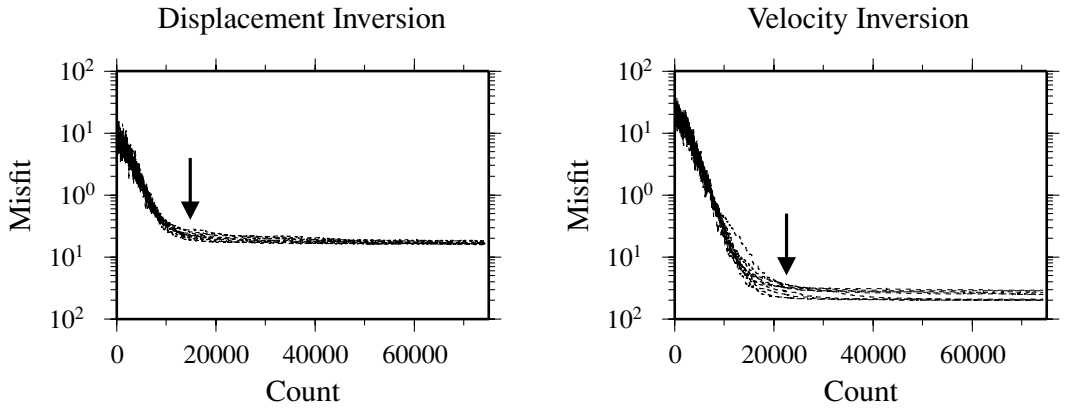

Fig. 10. Variations of the misfit functions with increasing iterations in the displacement and velocity inversions. Solid arrows indicate the points where the temperature reaches T_c.

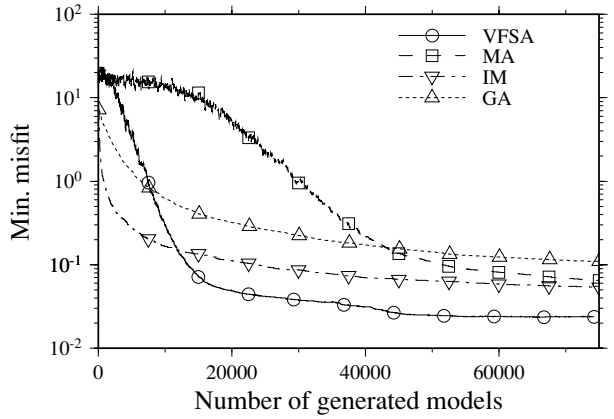

Fig. 11. Minimum misfit values obtained from the four different search algorithms, which are Metropolis algorithm (MA), iterative improvement method (IM) and genetic algorithm (GA). Horizontal axis indicates the number of generated models (i.e. calculation of ground motions)

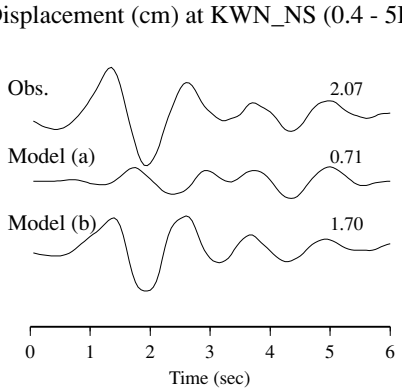

Fig. 12. Displacement waveforms on the NS component at KWN. Top trace shows the observed waveform. Middle and bottom traces show the synthetic waveforms from the model (a) and the model (b) respectively.

Table 3. Search areas of model parameters in application to the target event.

Displacement inversion		
C	a (s)	v/β
0.0–2.0	0.0–1.0	0.55–0.8

Velocity inversion		
C^0	C^1	v/β
0.0–2.0	0.0–5.0	0.55–0.8

of the misfits with different initial values is rather small. Temperature reaches the critical point T_c at about the 20th lowering in the displacement inversion and the 30th lowering in the velocity inversion in this numerical test, which correspond with 14,800 and 22,500 iterations respectively as indicated by arrows in Fig. 10.

Finally we attempted the same numerical tests by using the other heuristic techniques, which are the conventional Metropolis algorithm (MA), the iterative improvement method (IM) and the genetic algorithm (GA). The conventional MA means simulated annealing that searches a new parameter from the full search area uniformly. IM is the algorithm which accepts a new random parameter if and only if it provides a superior (small misfit) model. The number of model generations in GA is set to agree with that in VFSA. The elite selection to 10% of the best individuals and the dynamic mutation fluctuating from 1 to 10% are introduced in GA. The resultant minimum misfit values obtained from these four search algorithms are shown in Fig. 11 as a function of the number of examined models. As seen in Fig. 11 the misfit of VFSA falls slower than GA and IM until about 10,000 model generations due to the almost pure random search at high temperature. After that, however, VFSA can find better solutions compared with other methods as indicated by the lower misfit values. Since the iterative improvement moves to the model with smaller misfit straightforwardly, the misfit value reduces very rapidly in the early stage. But this method is likely to converge towards the local minima (Mosegaard and Vestergaard, 1991). The reduction of the misfit is slowest in conventional MA until more than half of the model realizations in the total iteration schedule are performed because of very slow cooling schedule. MA samples the parameters assuming a uniform distribution in the model space, so that milder cooling step is necessary to attain the global minimum. The performance of GA is not so good in this numerical test. Generally GA can find the area where the global minimum exists more easily than the family of SA. While once the point near the global minimum is found, the neighborhood search algorithm like VFSA is better for the local search (e.g. Reeves, 1993).

4.2 Application to the 1997 Izu-Hanto Toho-Oki Earthquake

We applied the VFSA inversion to the strong-motion records from the 1997 Izu-Hanto Toho-Oki Earthquake of MJMA 5.9. First we determined the suitable initial fault model from the models (a) and (b) as shown in Fig. 3. When the location of the initial fault model is inappropriate, ground motions at the station close to the fault such KWN are not often represented well. Here we performed the displacement inversion with two assumed fault models and compared the synthetic ground motions at KWN with observed one. In Fig. 12 we show the displacement motions of the NS component at KWN. Obviously the synthetic displacement motion based on the fault model (b) agrees well with the observed one compared to the synthetic motion with the model (a). In fact the inverted source model by using model (b) releases a large moment from the shallowest area as discussed later, which is not included in the model (a). Consequently we adopted the initial fault model (b) in this study.

We further examined a radiation pattern of the S wave at each observation station. Though the radiation pattern does not appear clearly in high frequency ground motions (e.g. Liu and Helmberger, 1985), the results from the displacement inversion might be influenced. In particular station KWN is located close to the target event so that the azimuth and take-off angle to the station vary with the position of the sub-faults. Moreover for the assumed fault geometry the EW component at KWN is nearly nodal for

Table 4. Comparison of the total seismic moment of the target event obtained by the VFSA displacement inversion with those determined from spectral analysis and by other researchers (F-net and Kikuchi (1997, on the web site))

	This study	Spectral analysis	F-net	Kikuchi (1997)
Total moment (Nm)	1.31×10^{17}	1.75×10^{17}	2.09×10^{17}	1.00×10^{17}

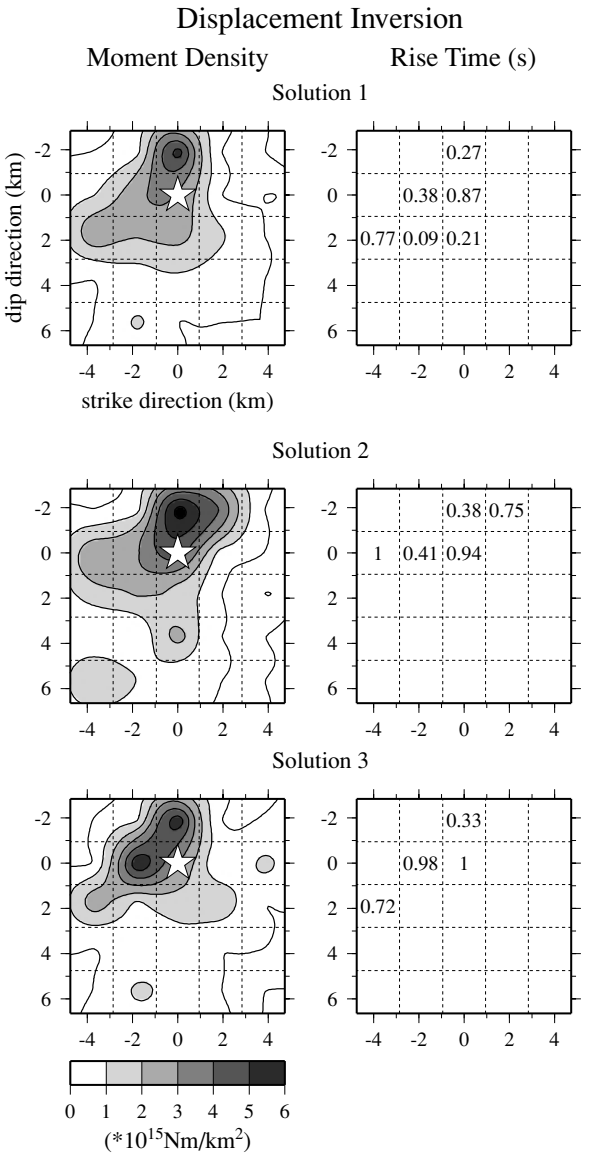

Fig. 13. The best three source models regarding the distributions of moment density and rise time for the target event for 10 solutions of the VFSA displacement inversions. Values of rise time are given only for the sub-faults where more than twice the average moment is released. An open star shows the hypocenter.

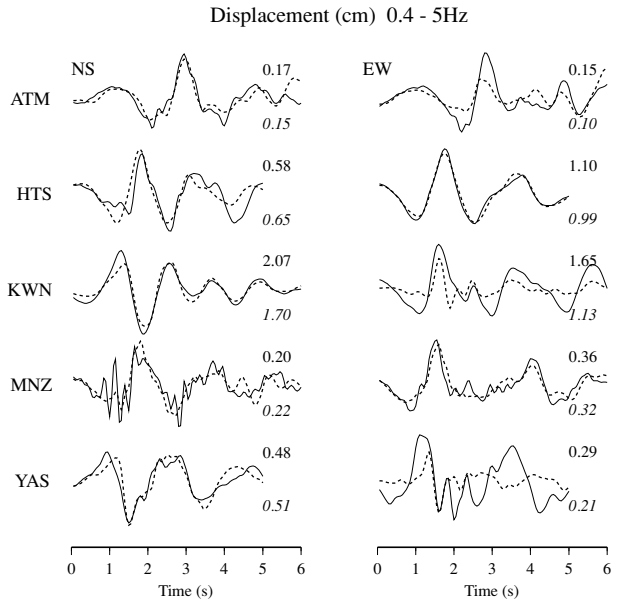

Fig. 14. Comparison of synthetic and observed displacement waveforms. Solid lines show the observed waveforms and broken lines denote synthetic ones. Numbers above the waveforms are the peak values of observed motions and those below the waveforms are the peak values of synthetics, respectively.

S waves. We found that the radiation patterns of the EW component at KWN from more than half of the sub-faults of the target event show the opposite sign to that from the element event. To correct such differences in the sign of radiation patterns we performed the displacement inversion with changing the sign of the element waveform of the EW component at KWN. However the resultant synthetic motion of the target event shows an almost reverse trace to the observed one, suggesting that the sign of the radiation pattern from the target event should be same as that from the element event for suitable waveform fittings. Since the EW component at KWN is close to the nodal for the target and element event, a small change in the fault geometry and/or lateral heterogeneity of subsurface structure might change the sign of radiation patterns. We also attempted the displacement inversion without the EW component of KWN. The obtained moment distribution is roughly coincides with the inversion results obtained by using full data. However the variance of the rupture times inferred from the inversion with different initial values becomes large due to a decrease in the number of data. Therefore we did not remove the EW component of KWN in the following analysis.

In Fig. 13 we show the best three solutions regarding the distributions of moment density and rise time of the target event obtained from 10 VFSA displacement inversions with different initial values for generation of random numbers. The search areas for parameters are shown in Table 3 for the displacement and velocity inversions. In the figure the rise times are filled in only the sub-faults where more than twice the average moment is released to eliminate the incorrect solutions at the low moment released area as seen in the numerical tests. We used the S-wave portion of two horizontal ground motions for the inversion. We performed preliminary inversions with different constant rupture velocities and determined the appropriate initial model for rupture velocity of 0.65 β that shows the minimum misfit at

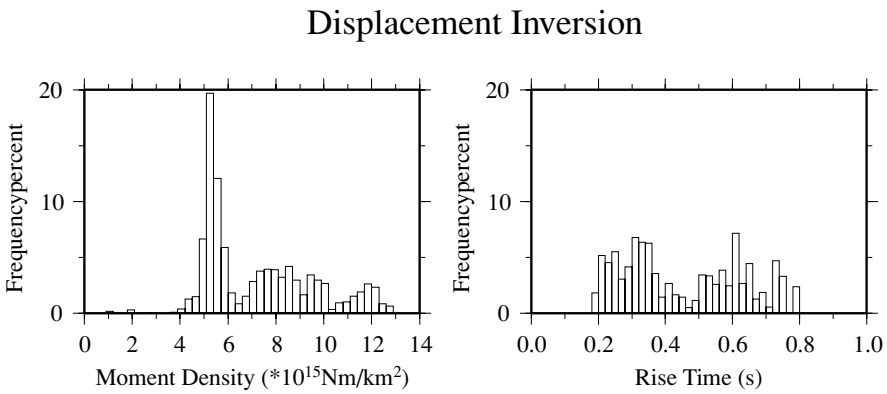

Fig. 15. Histograms of the a posteriori parameter distributions at the asperity mesh located just above the hypocenter sampled just below T_c from 10 displacement inversions. About 7,000 sampled models are plotted.

the end of inversion. The best three source models in Fig. 13 show similar moment distributions. The large moment released area is located in the shallow region just above the hypocenter and extends to the northern area (the left direction in the figure) of the hypocenter. The rise time distribution ranges from 0.3 to 1 second, showing large variations. In Table 4 we compare the total seismic moment obtained from the best three inversion results on average with the results from other studies, which are the spectral inversion (in this study) and the moment tensor inversion reported by F-net (Fukuyama *et al*., 1998) and Kikuchi (1997, on the web site). Our estimated seismic moment coincides well with other results. Figure 14 shows the synthetic displacement motions calculated from the best source model with the observed ones. The fit between them is generally good.

To see the most frequently sampled values in the inversion procedure, we show in Fig. 15 the histograms of the parameter distributions at the asperity mesh located just above the hypocenter, which are sampled just below the critical temperature from 10 inversions. The histogram of model parameters is interpreted as the marginal a posteriori distributions (Mosegaard and Tarantola, 1995; Ihmlé and Ruegg, 1997), and gives us the information of the reliability and the resolution of estimated solutions. As seen in Fig. 15, the histogram of sampled moment densities in the displacement inversion shows a distinct peak near 5×10^{15}Nm/km^2, while the sampled value of rise time distributes more extensively.

For the velocity inversion we also show the three best models within 10 inversions in Fig. 16. The rise times at the large moment-released meshes are fixed by averaging the three best results of displacement inversion. For other meshes where small or almost no moments are released in the displacement inversion, we assumed the constant value of 0.5 second. The moment distribution derived from the velocity inversion roughly corresponds to that from the displacement inversion shown in Fig. 13. However the total amount of the released moment is about 40% smaller than the result from the displacement inversion. The reason is that the velocity inversion might be insensitive to the low-frequency components that are directly related to the released moment, because the VFSA algorithm tends to fit higher-frequency motions more correctly in the velocity in-

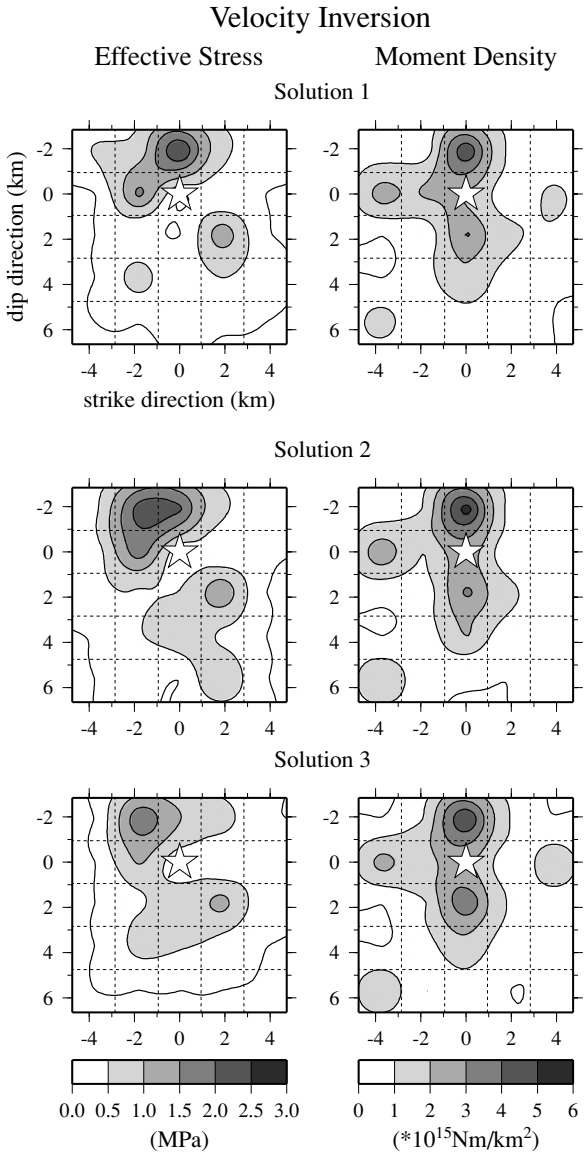

Fig. 16. The best three source models mapping the distributions of the effective stress and the seismic moment for 10 solutions of the VFSA velocity inversions. An open star shows the hypocenter.

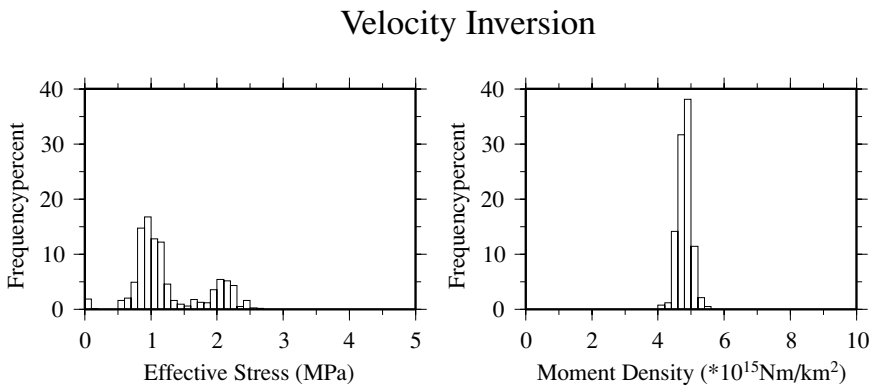

Fig. 17. Histograms of the a posteriori parameter distributions at the asperity mesh located just above the hypocenter sampled just below T_c obtained from 10 velocity inversions. The number of sampled models is roughly the same as that in the displacement inversion.

version. The distribution of the effective stress is similar to that of the moment release in the velocity inversion. This implies that radiation of the high-frequency waves share common areas with the release of the large moment, i.e. asperity.

In Fig. 17 we show the histograms of the parameter distributions obtained from the velocity inversion at the same mesh as the case of the displacement inversion. The distribution of the moment density is relatively well centered at the value being generally consistent with those estimated from the displacement inversion in Fig. 15, though the effective stress shows two peaks in the histogram.

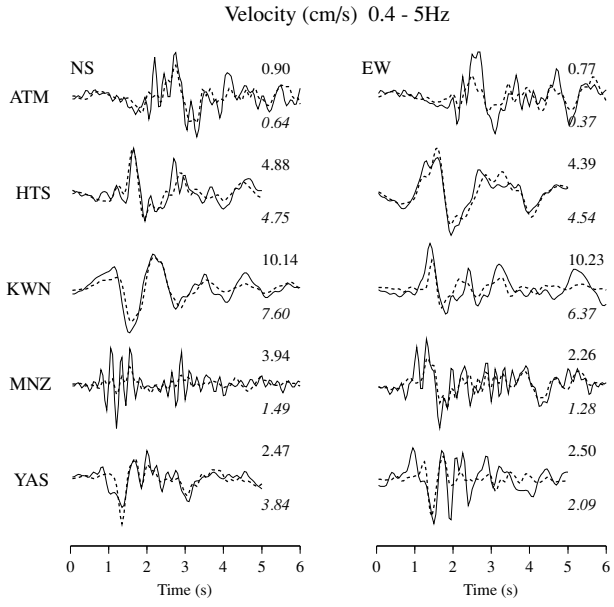

Fig. 18. Comparison of synthetic and observed velocity waveforms. Solid lines show the observed waveforms and broken lines denote synthetic ones. Numbers above the waveforms are the peak values of observed motions and those below the waveforms are the peak values of synthetics, respectively.

Figure 18 compares the synthetic velocity motions from the source model with the smallest misfit and the observed ones. The estimated source model reproduces the velocity motions rather well though it is still difficult to fit the high-frequency signals accurately.

Figure 19 shows the distribution of the rupture-time perturbation s_i for both the displacement and velocity inversions. We see the perturbation of the rupture time from the initial model with the constant rupture velocity is small and the rupture propagation is very smooth on the fault plane of the target event.

5. Discussion

5.1 Selection of the type of norm for calculation of misfit

In this study we minimize the L1 norm for the evaluation of the misfit during the displacement inversion. Generally the L2 norm is often employed for the measurement of misfit between observed data and models in the inversion procedure, because the L2 norm is used for maximizing the likelihood function that obeys the Gaussian distribution (Duijndam, 1988). It is well known that the Gaussian distribution approximates closely the behavior of errors of many measurements in physical problems. On the other hand the L1 norm is more robust having the property to be less sensitive to large outliers than the L2 norm. For instance Das and Kostrov (1990) solved the source inversion by using the linear programming method with the minimization of the L1 norm. They also evaluated the L2 norm and the L∞ norm (Chebyshev norm), and confirmed the L2 norm behaves in a similar manner than the L1 norm in their inversion procedure. It should be noted that minimizing the L1 norm signifies finding a median out of the noisy data, while the L2 norm minimization produces a mean value (Claerbout and Muir, 1973). In Fig. 20 we show the histogram of residuals derived from the L1 norm fitting in the displacement inversion and that from the L2 norm fitting in the velocity inversion respectively. Here the residual is normalized with the standard deviation σ such as $(u_S(t) - u_O(t))/\sigma$ for each station and component, where u_S and u_O are the synthetic and observed motions as shown in Eq. (13). In Fig. 20 both residuals obey the normal distribution with zero mean, which indicates the selection of the L1 norm as well as the L2 norm is appropriate in our problem.

Following Claerbout and Muir (1973), for the fitting problem to time series data, the L2 norm fitting is good near the sudden change or discontinuity of amplitude, while the L1 norm fitting is better than the L2 fitting away from the

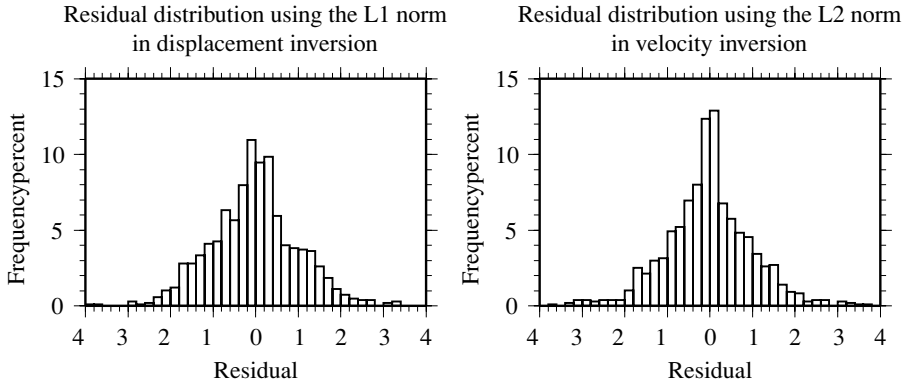

Fig. 20. Histogram of residuals derived from the L1 norm fitting in the displacement inversion (left) and that from the L2 norm fitting in the velocity inversion (right).

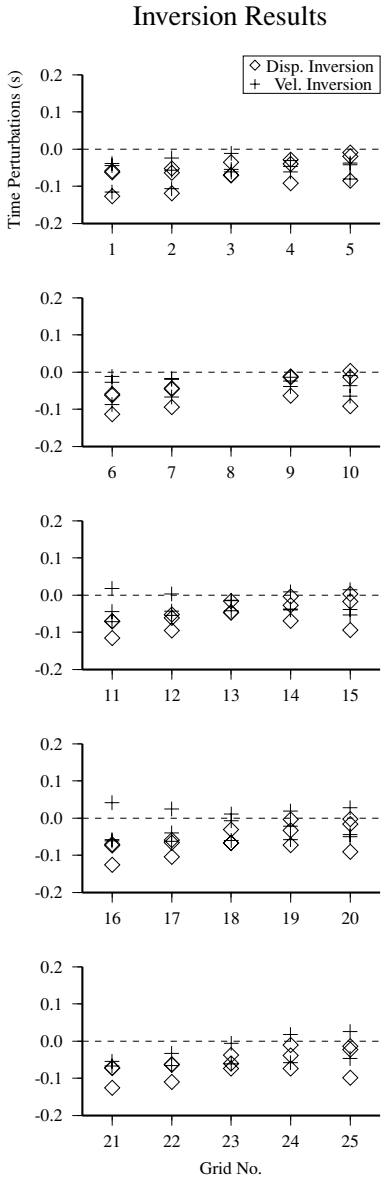

Fig. 19. Distribution of the rupture-time perturbation s_i for both the displacement and velocity inversions for the three best inversion results. Horizontal axis indicates the mesh number of the target fault, measured from the northern shallowest mesh along the strike direction.

major discontinuity. In our problem the L2 norm is appropriate for fitting the wave portion near the peak amplitude, and the L1 norm is able to fit the total waveforms at some cost to accuracy near the peak values. Since the rise time is considered to be more sensitive to total waveforms than individual peak amplitudes for long-period waves, it is appropriate to use the L1 norm for the displacement inversion. In contrast, it is important for the velocity inversion to fit several distinct peak amplitudes of high-frequency velocity motions in order to infer the spatio-temporal distribution of effective stress as well as the seismic moment. Therefore the L2 norm is better for the velocity inversion, though few differences were seen between the results of the L1 and L2 norm minimization in the numerical test.

5.2 Characterization of source model and broadband ground motion simulation

Characterizing the source models of the past earthquakes is useful for constructing the source models of future earthquakes for the prediction of strong ground motions as indicated by Somerville *et al*. (1999). They systematically analyzed slip models of past inland crustal earthquakes derived from the waveform inversions in the low frequency range, and found self-similar scaling of the slip heterogeneity such as the area of total asperity and that of the largest asperity with respect to seismic moment. Miyakoshi *et al*. (2000) inferred the slip variations of inland earthquakes of M6 class in Japan, and pointed out similar scaling relationships to the results by Somerville *et al*. (1999). Characterization of earthquake source models makes it possible to describe the heterogeneity of faulting process by the finite number of parameters, and it leads to the statistical analysis for specifying the scaling relations between earthquake size and the degree of fault roughness from the source models of past earthquakes. Therefore we can construct a statistically reliable source model for the future scenario earthquake through the source characterization procedure. However the source characterization using the results of waveform inversion so far has been done for low-frequency ground motions. On the other hand Miyake *et al*. (2003) estimated the "strong motion generation area" by fitting the displacement waveforms and acceleration envelopes simulated using the empirical Green's function method to observed data in the frequency range from 0.2 to 10 Hz. They used the forward

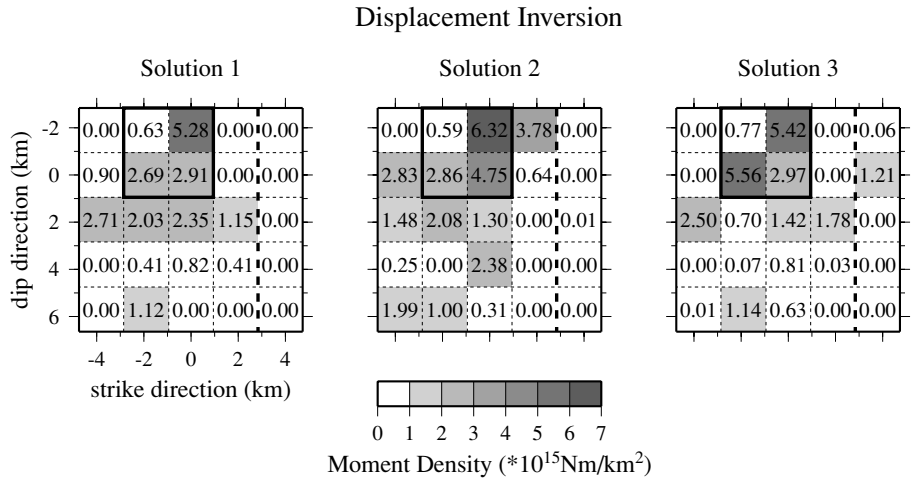

Fig. 21. Total rupture area and the area of asperity for the characterized source model identified from the three best solutions of the displacement inversion. The areas enclosed with the thick lines indicate the areas of asperity. The edges divided by the broken lines are removed to define the rupture area of the characterized source model.

modeling technique and found the sizes and positions of the strong motion generation area estimated from the strong ground motions in the broadband frequency range coincide with those of the characterized asperity derived from the low-frequency ground motions. Here we characterize the spatial variations of effective stress and released moment for the target event estimated by the VFSA inversion. Then the validity of the characterization scheme is confirmed by comparing the synthetic ground motions using characterized source model with the observed ones in the broadband frequency range up to 10 Hz, which is often required for an engineering purpose. The scaling relation of characterized source parameters with seismic moment is also compared with other studies.

First we identify the total rupture area and the asperity area of the target event from the moment distribution obtained using the displacement inversion. Somerville *et al*. (1999) proposed the way of determination of the objective rupture area by removing the edges with small slip values from the heterogeneous slip model. They also defined the identification of asperity based on the relative slip value in each sub-fault. We apply the criterion presented by Somerville *et al*. (1999) correspondingly to characterization of our inversion results, though we use the moment distribution as a substitute for the slip distribution. Figure 21 shows the total rupture area and the area of asperity we identified from the three best results of the displacement inversion. The edge column on the right side in Fig. 21 is trimmed due to small moment release. Then the rupture area of the characterized model is defined. The area of asperity is determined as the area composed of four sub-faults located near the hypocenter. The ratio of the asperity area to total rupture area is 0.2, which is consistent with the empirical relation of 0.22 deduced by Somerville *et al*. (1999). Figure 22 shows the relation between the area of asperity and the seismic moment of the target event and the comparison with the scaling proposed by Somerville *et al*. (1999) and Miyake *et al*. (2003). Note that the scaling relation proposed by Miyake *et al*. (2003) provides the strong motion generation area with respect to the seismic moment as mentioned above. Here we adopt the seismic moment of the target event determined from the moment tensor inversion by F-net (Fukuyama *et al*., 1998). The relation of asperity area to seismic moment shows a good agreement with the empirical scaling relations by Somerville *et al*. (1999) and Miyake *et al*. (2003).

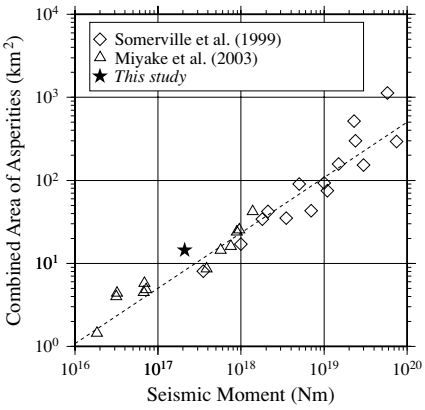

Fig. 22. Relation between the area of asperity and the seismic moment. Solid star shows the relation of the target event found in this study. Open diamonds and triangles are the combined area of asperities (Somerville *et al*., 1999) and the strong motion generation areas (Miyake *et al*., 2003), respectively. Broken line shows the scaling relation proposed by Somerville *et al*. (1999).

Next we derive the effective stress on the asperity and background area for the target event. Since the variation of effective stress has been estimated with the moment distribution from the velocity ground motions in the frequency range up to 5 Hz, we can use such information directly to deduce the characterized source model. The high-frequency ground motions radiated from several sub-faults are represented as an incoherent summation (Boatwright, 1988). Therefore the acceleration spectral ratio between the asperity of the target event and the element event in a sufficiently high frequency range (higher than the corner frequency of the element event) is expressed using the effective stress ra-

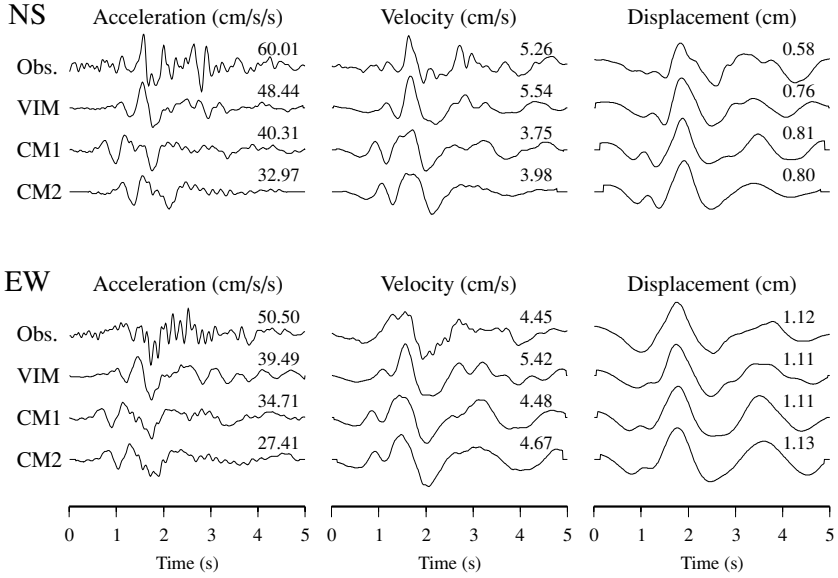

Fig. 23. Comparison between the synthetic ground motions from three source models and the observed ground motions at HTS. Number above each trace shows the peak value. "VIM" indicates the source model directly using the result of the velocity inversion. "CM1" is the characterized source model composed of only asperities, and "CM2" is that including asperities and background area.

Table 5. Parameters of the characterized source model for the target event.

Asperity			Background		
N_a	C_a	N_{Ta}	N_b	C_b	N_{Tb}
2	0.46	3.30	4	0.098	3.62

tio C_i^1 as,

$$\frac{A_0^a}{a_0} = \left\{ \sum_{i=1}^{N_L^a \times N_W^a} \left(C_i^1\right)^2 \right\}^{1/2}, \tag{18}$$

where A_0^a and a_0 are the high-frequency amplitude level of the acceleration spectrum for the asperity of the target event and the element event, respectively. N_L^a and N_W^a indicate the scaling factors concerning the fault length and width of the asperity area that we initially estimated. For the characterized source model A_0^a/a_0 is equal to $C_a N_a$, where C_a and N_a denote the effective stress ratio and the fault dimension ratio between the characterized asperity and the element event. Then we obtain the following relation,

$$C_a N_a = \left\{ \sum_{i=1}^{N_L^a \times N_W^a} \left(C_i^1\right)^2 \right\}^{1/2}. \tag{19}$$

The moment ratio of the asperity to the element event is represented using C_a and N_a as follows,

$$C_a N_a^3 = \frac{\sum_{i=1}^{N_L^a \times N_W^a} M_o^i}{m_o} \tag{20}$$

where M_o^i is the released moment from the i-th sub-fault and m_o is that from the element event. From Eqs. (19) and (20) the uniform effective stress ratio C_a and the fault dimension ratio N_a of the characterized asperity to the element event are estimated. (It should be noticed that the characterized asperity area N_a^2 not necessarily corresponds to the initial guess of $N_L^a \times N_W^a$.) Here we assume the area of high effective stress for the target event corresponds to the asperity area deduced from the results of the displacement inversion. Then we obtain $C_a = 0.46$ and $N_a = 2$, which results in the equal area to the initial assumption.

The effective stress ratio C_b on the background area surrounding the asperity is given by the following equations,

$$\begin{aligned} C_b N_b^3 &= \frac{\sum_i^{i \notin N_L^a \times N_W^a} M_o^i}{m_o} \\ N_b &= \sqrt{N^2 - N_a^2} \end{aligned} \tag{21}$$

where N and N_b are the scaling factor concerning the fault dimension of the total rupture area and background area respectively. The addition of seismic moments M_o^i in Eq. (21) is carried out at the sub-faults except for the initially assumed $N_L^a \times N_W^a$ asperity.

The total amount of the seismic moment is corrected using the results from the displacement inversion due to the underestimation of the seismic moment in the velocity inversion. The correction is made by changing the scaling factor concerning the slip duration time (or rise time) as follows,

$$C_a N_a^2 N_{Ta} = \frac{\sum_{i=1}^{N_L^a \times N_W^a} M_{od}^i}{m_o} \tag{22}$$

where N_{Ta} is the rise time ratio between characterized asperity and element event. M_{od}^i denotes the seismic moment of the i-th sub-fault estimated from the displacement inversion. Though Eq. (22) is valid for the characterized asperity area, a similar relation is valid for the background area to estimate the rise time ratio N_{Tb}.

The estimated parameters for the characterized source model of the target event, C_a, N_a and N_{Ta} for the asperity and C_b, N_b and N_{Tb} for the background area, are summarized in Table 5. They are obtained by averaging the results from the three best source models in the displacement and

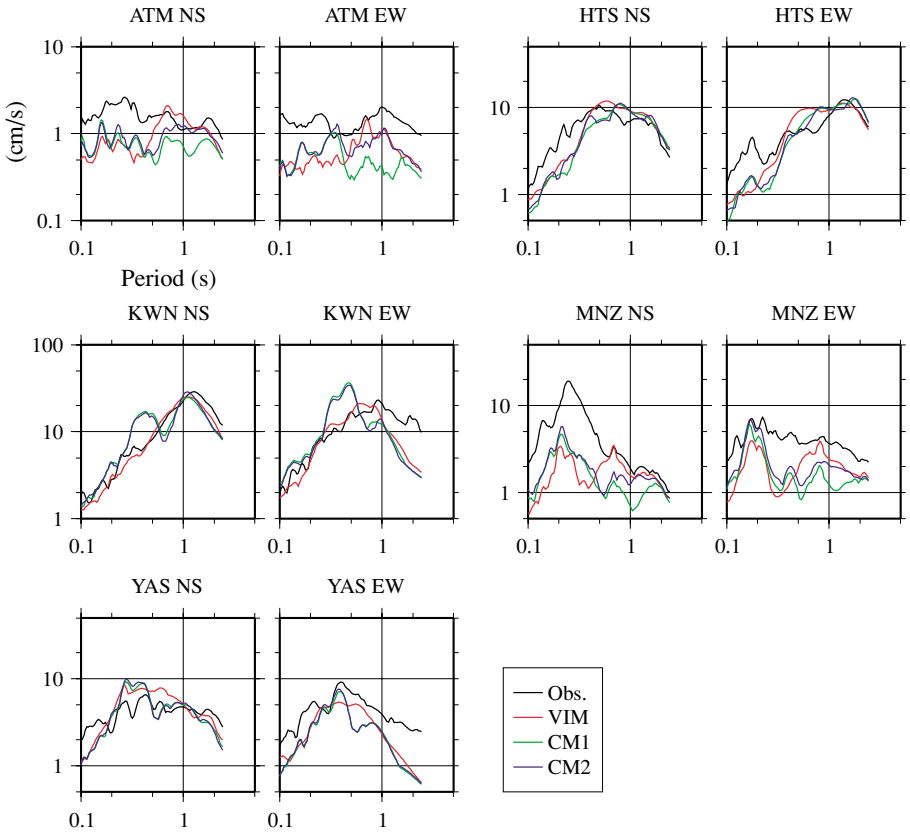

Fig. 24. Pseudo velocity response spectra with 5% damping calculated from the observed and three synthetic ground motions.

the velocity inversions. We obtain the effective stress ratio at asperity of 0.46 and that in the background area of 0.098. So the ratio of effective stress between the characterized asperity and the background area become approximately 0.2, which is as twice large as the solutions of numerical simulations based on the dynamic rupture model with single asperity (Irikura, 2004). Since the effective stress of the element event is estimated as 3.11 MPa (see Table 1), the effective stress on the asperity of the characterized source model becomes 1.43 MPa, which is very small compared with the average value of 10.5 MPa deduced by Irikura (2004). The moment release from the asperity occupies 52% of the total moment, which is slightly larger than the empirical relation of 44% (Somerville *et al.*, 1999) and the dynamic solution of single asperity model of 45.5% (Irikura, 2004), which might be due to the rough spatial division of the fault plane.

We calculate synthetic ground motions in the frequency range from 0.4 to 10 Hz with the EGF method based on three source models, i.e. the model using the results of velocity inversion directly, characterized source model with only the asperity and characterized source model with asperity and background area. The rise time is fixed to be 0.5 second over the entire fault and constant rupture velocity of 0.65 times the *S* wave velocity is assumed for all source models. Figure 23 shows the comparison between the synthetic ground motions from three source models and the observed ground motions at HTS as an example. The fit between the synthetic and observed ground motions are generally good for their peak values and envelope shapes, though detailed waveforms do not agree completely.

The pseudo velocity response spectra calculated from the observed and three synthetic ground motions are shown in Fig. 24. On the EW components at the stations of KWN and YAS the synthetic ground motions from all three models underestimate the low-frequency amplitudes compared with the observed motions as seen in Fig. 24. The EW components at KWN and YAS are nearly nodal for the *S*-waves from both the target and element events. As discussed before the radiation pattern on the EW component at these stations will vary with the position of the sub-fault for the target event if the hypocentral distance is short. The effect of the radiation pattern from the target event is therefore smoothed for the stations located in the direction of the fault normal, and hence the synthesized motion will be underestimated when the radiation pattern for the element event is small. The NS component at MNZ also shows a large discrepancy in the spectral amplitude between synthesized and observed motions. MNZ is relatively far from the hypocenter and is located in the direction close to the strike of the both events. Accordingly the amplitude of the synthesized ground motion on the NS component at MNZ is further sensitive to a small difference in the fault geometry between the target and small events. In fact, we can see the radiation pattern on the NS component for the element event is very small compared with that for the target event at the azimuth of MNZ. This might be the reason for the underestimation of the NS component at MNZ.

Figure 25 shows the cross-correlation coefficients and the residuals between the synthetic waveforms and the observed ones for velocity and displacement waveforms

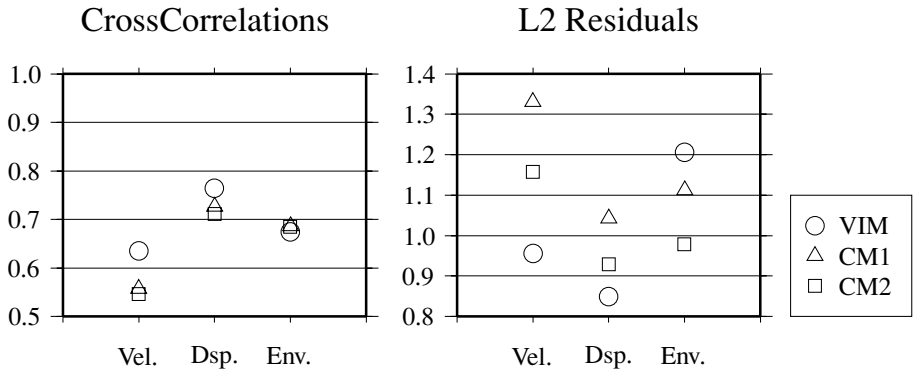

Fig. 25. Cross-correlations (left) and residuals (right) between the synthetic and observed waveforms.

with acceleration envelopes. The decrease of the cross-correlations and the increase of the residuals caused by the characterization of the source model from the velocity inversion are rather small except for the residual of the velocity motions, which is the objective function to be minimized during the VFSA inversion procedure.

6. Conclusions

A source inversion using very fast simulated annealing (VFSA) with the empirical Green's function method was proposed for estimating the rupture process radiating broadband ground motions. This inversion algorithm allows us to separately estimate the spatial distributions of the effective stress and seismic moment with the rupture time by inverting the velocity ground motions in the frequency range up to 5 Hz. From the displacement motions the released moment, rise time and rupture time are estimated. The developed inversion method was applied to the strong-motion data from the 1997 Izu-Hanto Toho-Oki earthquake (MJMA 5.9). Results of the displacement and velocity inversion exhibit the similar distribution of the seismic moment, in which the large moment released area is located in the shallow part just above the hypocenter and extends a little deeper to the northern area. The distribution of the effective stress deduced from the velocity inversion is similar to that of the moment release, suggesting that radiation of the high-frequency waves share common areas with the release of the large moment, i.e. asperity. We further displayed the procedure for constructing the characterized source model from the spatial distributions of the effective stress and the seismic moment obtained from the VFSA inversions. The validity of the procedure was confirmed by comparing the synthetic broadband ground motions from the characterized source models with those from the pre-characterized model, i.e. the results of the velocity inversion, and with the observed ground motions. We also compared our deduced parameters for the characterized source model with the empirical scaling relations proposed by other researchers, and found good agreement.

The VFSA inversion is appropriate for solving the nonlinear problems that have many local minima such as high-frequency waveform fittings. Our developed inversion scheme derives the spatio-temporal variations of the effective stress and seismic moment separately from the broadband-frequency velocity motions. Therefore based on the inversion results we can construct the characterized source model that contains the effects of high-frequency radiation from the earthquake source up to the frequency range used in the inversion procedure. From this point of view, the VFSA inversion method and the source characterization procedure we proposed in this paper contribute to the reliable source modeling for the prediction of strong ground motions by applying them to a number of past earthquakes and clarifying a common relation between the local variation of effective stress and that of released moment over the seismic fault.

Acknowledgments. We would like to thank the F-net operated by the National Research Institute for Earth Science and Disaster Prevention (NIED) for providing the moment tensor solutions, and Japan Meteorological Agency (JMA) for providing the hypocenter information for the earthquake event we analyze and its aftershocks. Constructive comments from Drs. P. M. Mai and E. Fukuyama, and an anonymous reviewer are greatly appreciated to improve the manuscript. We used Generic Mapping Tools (Wessel and Smith, 1995) to draw several figures in this paper.

References

Aki, K., Scaling law of seismic spectrum, *J. Geophys. Res.*, **72**, 1217–1231, 1967.

Boatwright, J., The seismic radiation from composite models of faulting, *Bull. Seism. Soc. Am.*, **78**, 489–508, 1988.

Boore, D. M., Stochastic simulation of high frequency ground motion based on seismological models of radiated spectra, *Bull. Seism. Soc. Am.*, **73**, 1865–1894, 1983.

Brune, J., Tectonic stress and the spectra of seismic shear waves from earthquakes, *J. Geophys. Res.*, **75**, 4997–5009, 1970.

Brune, J., Correction, *J. Geophys. Res.*, **76**, 5002, 1971.

Claerbout, J. F. and F. Muir, Robust modeling with erratic data, *Geophysics*, **38**, 826–844, 1973.

Das, S. and B. V. Kostrov, Inversion for seismic slip rate history and distribution with stabilizing constraints: Application to the 1986 Andreanof Islands earthquake, *J. Geophys. Res.*, **95**, 6899–6913, 1990.

Day, S. M., Three-dimensional finite difference simulation of fault dynamics; rectangular faults with fixed rupture velocity, *Bull. Seism. Soc. Am.*, **72**, 705–727, 1982.

Delous, B., P. Lundgren, J. Salichon, and D. Giardini, Joint inversion of InSAR and teleseismic data for the slip history of the 1999 Izmit (Turkey) earthquake, *Geophys. Res. Lett.*, **27**, 3389–3392, 2000.

Delous, B., D. Giardini, P. Lundgren, and J. Salichon, Jointinversion of InSAR, GPS, teleseismic, and strong-motion data for the spatial and temporal distribution of earthquake slip: Application to the 1999 Izmit Mainshock, *Bull. Seism. Soc. Am.*, **92**, 278–299, 2002.

Duijndam, A. J. W., Baysian estimation in seismic inversion. Part I: Principles, *Geophysical Prospecting*, **36**, 878–898, 1988.

Eshelby, J. D., The determination of the elastic field of an ellipsoidal inclusion and related problems, *Proc. Roy. Soc. Lond.*, A, **241**, 376–396, 1957.

Fukuyama, E., Inversion for the rupture details of the 1987 east Chiba earthquake, Japan, using a fault model based on the distribution if relocated aftershocks, *J. Geophys. Res.*, **96**, 8205–8217, 1991.

Fukuyama, E. and K. Irikura, Heterogeneity of the 1980 Izu-Hanto-toho-Oki earthquake rupture process, *Geophys. J. Int.*, **99**, 711–722, 1989.

Fukuyama, E., M. Ishida, D. S. Dreger, and H. Kawai, Automated seismic moment tensor determination by using on-line broadband waveforms, *Zisin* 2 (J. Seism. Soc. Japan), **51**, 149–156, 1998 (in Japanese with English abstract).

Geman, S. and D. Geman, Stochastic relaxation, Gibbs distribution, and the Bayesian restoration of images, *IEEE Trans. Patt. Anal. Mach. Int.*, **6**, 721–741, 1984.

Gibert, D. and J. Virieux, Electromagnetic imaging and simulated annealing, *J. Geophys. Res.*, **96**, 8057–8067, 1991.

Hartzell, S. H., Earthquake aftershocks as Green's functions, *Geophys. Res. Lett.*, **5**, 1–4, 1978.

Hartzell, S. H. and T. H. Heaton, Inversion of strong ground motion and teleseismic waveform data for the fault rupture history of the 1979 Imperial Valley, California earthquake, *Bull. Seism. Soc. Am.*, **73**, 1553–1583, 1983.

Hellweg, M. and J. Boatwright, Mapping the rupture process of moderate earthquakes by inverting accelerograms, *J. Geophys. Res.*, **104**, 7319–7328, 1999.

Holland, J. H., *Adaptation in Natural and Artificial Systems*, MIT Press, Cambridge, Massachusetts, 1975.

Horikawa, H., Earthquake doublet in Kagoshima, Japan: Rupture of asperities in a stress shadow, *Bull. Seism. Soc. Am.*, **91**, 112–127, 2001.

Ide, S., Source process of the 1997 Yamaguchi, Japan, earthquake analyzed in different frequency bands, *Geophys. Res. Lett.*, **26**, 1973–1976, 1999.

Ide, S., Complex source process and the interaction of moderate earthquakes during the earthquake swarm in the Hida-Mountains, Japan, 1998, *Tectonophysics*, **334**, 35–54, 2001.

Ide, S. and M. Takeo, Determination of constitutive relations of fault slip based on seismic wave analysis, *J. Geophys. Res.*, **102**, 27379–27391, 1997.

Ihmlé, P. F., Monte Carlo slip inversion in the frequency domain: Application to the 1992 Nicaragua slow earthquake, *Geophys. Res. Lett.*, **9**, 913–916, 1996.

Ihmlé, P. F., and J. C. Ruegg, Source tomography by simulated annealing using broad-band surface waves and geodetic data: Application to the Mw=8.1 Chile 1995 event, *Geophys. J. Int.*, **131**, 146–158, 1997.

Ingber, L., Very fast simulated re-annealing, *Mathl. Comput. Modelling*, **12**, 967–973, 1989.

Irikura, K., Semi-empirical estimation of strong ground motions during large earthquakes, *Bull. Disas. Prev. Res. Inst., Kyoto Univ.*, **33**, 63–104, 1983.

Irikura, K., Prediction of strong acceleration motions using empirical Green's function, *Proc. 7th Japan Conf. Earthq. Eng.*, 151–156, 1986.

Irikura, K., Recipe for predicting strong ground motion from future large earthquake, *Annuals of Disas. Prev. Res. Inst., Kyoto Univ.*, **47**, A, 2004 (in Japanese with English abstract).

Iwata, T. and K. Irikura, Source parameters of the 1983 Japan Sea earthquake sequence, *J. Phys. Earth*, **36**, 155–184, 1988.

Japan Meteorological Agency, Seismic activity in and around the Izu Peninsula (Novenber, 1996–April, 1997), *Rep. Coord. Comm. Earthq. Pred.*, **58**, 229–238, 1997 (in Japanese).

Ji, C. D., J. Wald, and D. V. Helmberger, Source description of the 1999 Hector Mine, California, earthquake, Part I: Wavelet domain inversion theory and resolution analysis, *Bull. Seism. Soc. Am.*, **92**, 1192–1207, 2002a.

Ji, C. D., J. Wald, and D. V. Helmberger, Source description of the 1999 Hector Mine, California, earthquake, Part II: Complexity of slip history, *Bull. Seism. Soc. Am.*, **92**, 1208–1226, 2002b.

Kakehi, Y. and K. Irikura, Estimation of high-frequency wave radiation areas on the fault plane by the envelope inversion of acceleration seismograms, *Geophys. J. Int.*, **125**, 892–900, 1996.

Kamae, K. and K. Irikura, Source model of the 1995 Hyogo-ken Nanbu earthquake and simulation of near-source ground motion, *Bull. Seism. Soc. Am.*, **88**, 400–412, 1998.

Kanamori, H. and D. L. Anderson, Theoretical basis of some empirical relations in seismology, *Bull. Seism. Soc. Am.*, **65**, 1073–1095, 1975.

Kinoshita, S., Frequency-dependent attenuation of shear waves in the crust of southern Kanto area, Japan, *Bull. Seismol. Soc. Am.*, **84**, 1387–1396, 1994.

Kirkpatrick, S., C. D. Gelatt, and M. P. Vecchi, Optimization by simulated annealing, *Science*, **220**, 671–680, 1983.

Liu, H. L. and D. V. Helmberger, The 23:29 aftershock of the 15 October 1979 Imperial Valley earthquake: More evidence for an asperity, *Bull. Seism. Soc. Am.*, **75**, 689–708, 1985.

Mai, P. M. and G. C. Beroza, Source scaling properties from finite-fault rupture models, *Bull. Seism. Soc. Am.*, **90**, 604–615, 2000.

Metropolis, N., A. W. Rosenbluth, M. N. Rosenbluth, A. H. Teller, and E. Teller, Equation of state calculations by fast computing machines, *J. Chem. Phys.*, **21**, 1087–1092, 1953.

Miyake, H., T. Iwata, and K. Irikura, Strong ground motion simulation and source modeling of the Kagoshima-ken Hokuseibu earthquakes of March 26 (MJMA 6.5) and May 13 (MJMA 6.3), 1997, using empirical Green's function method, *Zisin* 2 (J. Seism. Soc. Japan), **51**, 431–442, 1999 (in Japanese with English abstract).

Miyake, H., T. Iwata, and K. Irikura, Source characterization for broadband ground-motion simulation: Kinematic heterogeneous source model and strong motion generation area, *Bull. Seism. Soc. Am.*, **93**, 2531–2545, 2003.

Miyakoshi, K., T. Kagawa, H. Sekiguchi, T. Iwata, and K. Irikura, Source characterization of inland earthquakes in Japan using source inversion results, *Proc. 12th World Conf. Earthq. Eng.*, 1850, 2000.

Mori, J. and S. Hartzell, Source inversion of the 1988 Upland, California, earthquake: Determination of a fault plane for a small event, *Bull. Seism. Soc. Am.*, **80**, 507–518, 1990.

Mosegaard, K. and A. Tarantola, Monte Carlo sampling of solutions to inverse problems, *J. Geophys. Res.*, **100**, 12431–12447, 1995.

Mosegaard, K. and P. D. Vestergaard, A simulated annealing approach to seismic model optimization with sparse prior information, *Geophys. Prospect.*, **39**, 599–611, 1991.

Nakahara, H., T. Nishimura, H. Sato, M. Ohtake, S. Kinoshita, and H. Hamaguchi, Broadband source rupture process of the 1998 Iwate Prefecture, Japan, earthquake as revealed from inversion analysis of seismic waveforms and envelopes, *Bull. Seism. Soc. Am.*, **92**, 1708–1720, 2002.

Okada, T., N. Umino, T. Matsuzawa, A. Hasegawa, and M. Kamiyama, Source processes of 15 September 1998 M5.0 Sendai, NE Japan, earthquake and its M3.8 foreshock by waveform inversion, *Bull. Seism. Soc. Am.*, **91**, 1607–1618, 2001.

Olson, A. H. and R. J. Aspel, Finite Faults and inverse theory with application to the 1979 Imperial Valley earthquake, *Bull. Seism. Soc. Am.*, **72**, 1969–2001, 1982.

Reeves, C. R., *Modern Heuristic Techniques for Combinatorial Problems*, McGraw-Hill, 1993.

Sekiguchi, H., K. Irikura, T. Iwata, Y. Kakehi, and M. Hoshiba, Minute locating of fault planes and source process of the 1995 Hyogo-ken Nanbu, Japan, earthquake from the waveform inversion of strong ground motion, *J. Phys. Earth*, **44**, 473–487, 1996.

Somerville, P. G., K. Irikura, R. Graves, S. Sawada, D. Wald, N. Abrahamson, Y. Iwasaki, T. Kagawa, N. Smith, and A. Kowada, Characterizing crustal earthquake slip models for the prediction of strong ground motion, *Seism. Res. Lett.*, **70**, 59–80, 1999.

Takeo, M., Rupture process of the 1980 Izu-Hanto-Toho-Oki earthquake deduced from strong motion seismograms, *Bull. Seism. Soc. Am.*, **78**, 1074–1091, 1988.

Trifunac, M. D., A three dimensional dislocation model for the San Fernando, California earthquake of February 9, 1971, *Bull. Seism. Soc. Am.*, **64**, 149–172, 1974.

Wessel, P. and W. H. F. Smith, New version of the Generic Mapping Tools released, *Eos Trans. Am. Geophys. Union*, **76**, 329, 1995.

Yamanaka, H., Application of simulated annealing to inversion of surface wave phase velocity—Comparison of performances between SA and GA inversions, *Butsuri-Tansa a(Geophys. Explor.)*, **54**, 197–206, 2001 (in Japanese with English abstract).

Yoshida, S. and K. Koketsu, Simultaneous inversion of waveform and geodetic data for rupture process of the 1984 Naganoken-Seibu, Japan, earthquake, *Geophys. J. Int.*, **103**, 355–362, 1990.

Zeng, Y., K. Aki, and T. Teng, Mapping of the high-frequency source radiation for the Loma Prieta earthquake, California, *J. Geophys. Res.*, **98**, 11981–11993, 1993.

Y. Shiba (e-mail: cbar@criepi.denken.or.jp) and K. Irikura